Published in final edited form as:

Nat Struct Mol Biol. 2019 December ; 26(12): 1176–1183. doi:10.1038/s41594-019-0343-6.

Structural basis of antagonism of human APOBEC3F by HIV-1 Vif

Yingxia Hu[1], **Belete A. Desimmie**[2], **Henry C. Nguyen**[1,3], **Samantha J. Ziegler**[1], **Tat Cheung Cheng**[1,4], **John Chen**[2], **Jia Wang**[5], **Hongwei Wang**[5], **Kai Zhang**[1], **Vinay K. Pathak**[2,*], **Yong Xiong**[1,*]

[1]Department of Molecular Biophysics and Biochemistry, Yale University, New Haven, Connecticut 06511, USA

[2]Viral Mutation Section, HIV Dynamics and Replication Program, Center for Cancer Research, National Cancer Institute at Frederick, Frederick, Maryland 21702, USA

[3]Present address: Department of Biochemistry and Biophysics, University of California, San Francisco, San Francisco, California 94158, USA

[4]Present address: IGBMC, CNRS, Illkirch 67404, France

[5]School of Life Sciences, Tsinghua University, Haidian District, Beijing 100084, China

Abstract

HIV-1 Vif promotes degradation of the antiviral APOBEC3 (A3) proteins through the host ubiquitin-proteasome pathway to enable viral immune evasion. Disrupting Vif-A3 interactions to reinstate the A3-catalyzed suppression of HIV-1 replication is a potential approach for antiviral therapeutics. However, the molecular mechanisms by which Vif recognizes A3 proteins remain elusive. Here we report a cryo-EM structure of the Vif-targeted C-terminal domain of human A3F in complex with HIV-1 Vif and its cellular cofactor CBFβ, at 3.9 Å resolution. The structure shows that Vif and CBFβ form a platform to recruit A3F, revealing a direct A3F-recruiting role of CBFβ beyond Vif stabilization, and captures multiple independent A3F-Vif interfaces. Together with our biochemical and cellular studies, our structural findings establish the molecular determinants that are critical for Vif-mediated neutralization of A3F and provide a comprehensive framework of how HIV-1 Vif hijacks the host protein degradation machinery to counteract viral restriction by A3F.

*Corresponding authors. All correspondence should be addressed to: yong.xiong@yale.edu or pathakv@mail.nih.gov.

Author contributions

Y.X., V.K.P., Y.H., B.A.D. designed the experiments. Y.H. performed the biophysical and biochemical experiments, B.A.D. performed the virological experiments. Data were analyzed by Y.X., Y.H., V.K.P., B.A.D.; H.C.N., S.J.Z., T.C.C., J.C., J.W., H.W., K.Z. contributed to experiments and discussions. Y.X., Y.H., V.K.P., B.A.D. wrote the paper.

Competing interests

All authors declare no competing financial interests.

INTRODUCTION

The apolipoprotein B mRNA editing catalytic polypeptide-like 3 (APOBEC3, A3) family of proteins are host intrinsic immunity factors that potently restrict a wide variety of viruses, including human immunodeficiency virus type 1 (HIV-1). As deaminases, A3 enzymes convert cytosine to uracil in the minus strand of viral single-stranded DNA (ssDNA) during reverse transcription, causing lethal hypermutation in the viral genome [1–3]. To evade this host defense, HIV-1 virion infectivity factor (Vif), facilitated by the cellular cofactor core-binding factor beta (CBFβ) [4,5], hijacks a host Cullin-RING E3 ubiquitin ligase complex to target A3s for proteasomal degradation [6–10]. Humans express seven A3 proteins that are homologous in sequence and structure, each containing one or two zinc-containing deaminase-like domains [11]. The di-domain A3s normally have only their C-terminal domain (CTD) catalytically active while their N-terminal domain (NTD) is responsible for encapsidation [12]. Of these, A3G and A3F are the most efficient restrictors of HIV-1 [13]. They interact with HIV-1 Vif through distinct domains, NTD for A3G and CTD for A3F [14–17]. Although the two domains are structurally conserved, they are proposed to interact with Vif via two separate interfaces [18,19]. Similarly, Vif is predicted to rely on different, partially overlapping motifs from three clustered regions to recognize A3G and A3F [18,20].

The Vif-hijacked E3 ubiquitin ligase is composed of the scaffold protein Cullin5 (Cul5), the E2-binding Rbx2, and adaptor proteins Elongin B (EloB) and Elongin C (EloC) [9], while the specific cofactor CBFβ plays a critical role in stabilizing Vif and its assembly with the ligase [21,22]. Although the recent crystal structure of the Vif-containing E3 ligase provided the molecular details of this Vif hijacking event [23], the fundamental question regarding how Vif recruits A3s to the E3 ligase remains unelucidated due to the absence of a Vif-A3 complex structure.

Here we present the cryo-EM structure of A3F CTD in complex with Vif and CBFβ, which reveals the structural basis of how Vif and CBFβ recruit A3F to the E3 ligase complex. This structure, together with our biochemical and virological mutagenesis observations, provides new insights into the molecular mechanism of Vif-mediated degradation of A3s.

RESULTS

Vif and CBFβ form a platform for interaction with A3F

We overcame various technical challenges to obtain cryo-EM reconstructions of Vif–A3F complexes (Fig.1). We first assembled a 7-component Vif–CBFβ–Cul5–EloB–EloC–Rbx2–$A3F_{CTD}$ complex by fusing a previously well characterized A3F CTD with solubility-enhancing mutations [24] (referred to as $A3F_{CTDm}$ hereafter for simplicity, see Methods) and CBFβ, which produced unreliable 3D reconstructions due to problems involving preferred particle orientations and flexible A3F binding. We then investigated the ternary Vif–CBFβ–$A3F_{CTDm}$ complex containing the same fusion. Interestingly, it stabilized a weak tetrameric form of the unfused ternary complex (Extended Data Fig. 1a). This tetramer complex is likely capturing multiple Vif–A3F interfaces, as a consequence of *in vitro* complex formation. The three-dimensional (3D) cryo-EM reconstruction of this complex at 5 Å resolution showed flexible regions including the Vif α-domain [23] protruding away from its

molecular core and the corresponding interacting CBFβ C-terminal regions (Fig. 1c and Extended Data Fig. 2a), whose removal improved the 3D reconstruction to 3.9 Å resolution without affecting the complex architecture (Extended Data Fig. 2b, right) and allowed reliable model building (Table 1, Fig. 1a and Extended Data Fig. 2b, left).

Strikingly, Vif and CBFβ together provide a rigid platform by forming two sides of a shallow wedge-like structure, and $A3F_{CTDm}$ lodges into the wedge mainly through its α-helical surface (α2, α3, and α4) (Fig. 1b). The catalytic site of A3F is located on the other end of the α-helices away from the interface (Fig. 1b). The interactions between Vif–CBFβ and $A3F_{CTDm}$ bury a surface area of 1004 $Å^2$. CBFβ, which was previously postulated to partially block A3F-binding motifs and need to be displaced for Vif-A3F interaction [18,21], in fact does not change the conformation of how it associates with Vif at all upon A3F binding. Instead it directly interacts with A3F, with its overall conformation and interaction with Vif largely unperturbed. Therefore, CBFβ not only serves as a critical cofactor stabilizing Vif and its assembly with the Cul5-E3 ligase [21,22], but also directly participates in A3F recruitment.

Both Vif–CBFβ and $A3F_{CTDm}$ maintain their overall architectures upon ternary complex formation (Fig. 1d). $A3F_{CTDm}$ undergoes little conformational changes upon binding to Vif-CBFβ (RMSD ~0.8 Å). Similarly, the majority of Vif and CBFβ remain structurally rigid (overall RMSD ~1.3 Å), with only a slight relative orientation shift between the two upon $A3F_{CTDm}$ binding (Extended Data Fig. 3). The largest local conformational change occurs in the Vif β4-β5 loop at the edge of the Vif/CBFβ interface (Fig. 1d, inset), which is mostly disordered in the reported Vif-E3 ligase structure [23]. This loop flips towards the Vif core to contact A3F, in a conformation further stabilized by the C-terminal region of Vif. Residues in this loop have been shown to be critical for A3F degradation [25–28]. This interaction also highlights the contribution of the Vif C-terminal region in recruiting A3F and explains its importance in neutralizing A3F [27,29]. For $A3F_{CTDm,}$ the major local conformational change occurs in loops located on the opposite side of the interaction interface (Fig. 1d), which is a result of a packing interaction from a neighboring Vif molecule in the tetramer complex (Extended Data Fig. 4a, left). These observations demonstrate that Vif and CBFβ can associate into a preformed structure poised to recognize A3F with minor structural adjustments.

Biological importance of the CBFβ-A3F interface

The newly identified interaction between CBFβ and A3F plays a pivotal role in Vif antagonization of A3F. This interface is primarily stabilized by electrostatic interactions between CBFβ residues F32-E54 and the C-terminal regions of $A3F_{CTDm}$ α3 and α4 helices (Fig. 2a). These A3F residues were previously considered to interact with Vif [16,27,30–32]. Particularly, CBFβ residues R35 and R43 create a strong positively charged surface abutting a large negatively charged surface at the C-termini of the α3 and α4 helices of $A3F_{CTDm}$, formed by E324 and multiple main chain carbonyls (Fig. 2b, top). Similarly, the negatively charged CBFβ E54 interacts with the positively charged A3F R293, whose conformation is further stabilized by Vif H73 (Fig. 2b, lower). Mutating any of these residues effectively disrupted the binding between the Vif–CBFβ–EloB–EloC complex and $A3F_{CTDm}$ *in vitro*

(Fig. 2c), rendered A3F resistant to Vif-mediated degradation in cells, and inhibited viral infectivity even in the presence of HIV-1 Vif (Fig. 2d). Remarkably, the charge swapped CBFβ E54K/$A3F_{CTDm}$ R293D double mutation rescued the complex formation *in vitro* (Fig. 2c), restored the Vif-mediated degradation of $A3F_{R293D}$ *in vivo*, and reestablished the viral infectivity against the otherwise Vif-resistant $A3F_{R293D}$ mutant (Fig. 2d), confirming that CBFβ E54 and A3F R293 are physically interacting. These data firmly validate the importance of the observed CBFβ-A3F interface in Vif-mediated degradation of A3F and enhancement of viral infectivity.

The observed CBFβ interface appears to uniquely interact with A3F, but not A3G. The same CBFβ mutations (R35E/R43E or E54K), which had critical effects on A3F, did not affect the Vif interaction with a solubility-enhanced A3G chimera construct (referred to as $A3G_{rh\text{-}hu}$, see Methods) *in vitro* (Fig. 2c), Vif-mediated human A3G degradation *in vivo*, or Vif-enhanced infectivity in the presence of A3G (Fig. 2e). The fact that these CBFβ mutants are functional against A3G also demonstrates that the mutations do not impair protein folding or the functional interactions between Vif and CBFβ, substantiating the direct role of CBFβ in A3F degradation. CBFβ has been found to be required for the expression of the A3 gene repertoire [33]. It is intriguing to speculate about the intrinsic cellular function of the A3F-CBFβ interaction at the protein level; however, their direct association in the absence of Vif was not detected *in vitro* or *in vivo* (Extended Data Fig. 1b,c). In contrast, a substantially enhanced interaction between A3F and CBFβ was found in cells in the presence of Vif (Extended Data Fig. 1c), demonstrating the importance of Vif for mediating the A3F-CBFβ interaction.

Biological importance of the Vif-A3F interface

The observed interface between HIV-1 Vif and A3F is also essential for viral evasion of A3F restriction. The Vif-$A3F_{CTDm}$ interface is mainly formed between two helices (α2 and α3) of $A3F_{CTDm}$ and multiple loop regions of Vif on the opposite side of its Cul5/EloC binding interface [23] (Fig. 3a, left and 4b). Both electrostatic and hydrophobic interactions are involved in stabilizing the interface (Fig. 3a, right). Specifically, a major stacking interaction occurs between Vif W79 and A3F P265 (Fig. 3b, left), which causes the aforementioned large conformational change of the Vif β4-β5 loop (Fig. 1d). Vif H80, which stacks with W79 in the absence of A3F (Fig. 1d), flips away to release W79 for A3F interaction (Fig. 3b, left top). W79, whose conformation is further stabilized by W174 at the Vif C-terminus, forms a small hydrophobic cleft with L81 to anchor A3F P265 (Fig. 3b, left lower). A modest stacking interaction also occurs between Vif W70 and A3F L255 (Fig. 3a). Besides hydrophobic interactions, two important electrostatic interactions occur at the interface. First, Vif R15 forms a strong interaction with the negatively charged main-chain carbonyls of A3F residues 260–263 located at the C-terminus of helix α2, whose α-helix dipole effect results in a net negative charge further contributing to the interaction with R15 (Fig. 3b, middle). Second, Vif K50, together with CBFβ E54 at the Vif/CBFβ interface, engages in electrostatic interactions with A3F E289 and R293, respectively, forming a ternary interface of the three proteins (Fig. 3b, right).

We also validated the biological relevance of the observed Vif-A3F interface. As expected, the W79A/H80A double mutation of Vif completely abolished its A3F binding capacity *in vitro* (Fig. 3c), while greatly inhibiting the A3F degradation and restricting viral infectivity *in vivo* (Fig. 3d). The A3F P265A mutant was partially resistant to Vif recognition and degradation (Fig. 3c,e). Demonstrating the importance of the electrostatic interactions, A3F E289K lost the ability to bind Vif, conferred resistance against Vif-mediated degradation, and retained viral restriction in the presence of Vif (Fig. 3c,f). Furthermore, the Vif R15D/E and K50E mutants were also severely defective in binding and neutralizing A3F (Fig. 3c,d,f,g). Consistent with the observed main chain and helix dipole interactions (Fig 3b, middle), the A3F D260R/D261R mutation had no effect *in vitro* or *in vivo* (Extended Data Fig. 5). In contrast to the effects on A3F, both Vif W79A/H80A and R15E mutants retained the ability to bind $A3G_{rh\text{-}hu}$ *in vitro* (Fig. 3c). The Vif K50E mutant had impaired binding efficiency to $A3G_{rh\text{-}hu}$ *in vitro* (Fig. 3c), which, however, was still sufficient to induce the degradation of human A3G *in vivo* (Extended Data Fig. 6).

The major Vif-$A3F_{CTDm}$ interface described above is located within one ternary complex, which further docks onto neighboring molecules in the observed tetramer through two other much smaller inter-ternary complex interfaces (Extended Data Fig. 4a), which have been implicated in A3F binding by several mutagenesis studies [20,25,27,28,34,35]. One such interface involves the Vif α1 helix close to the major interface (Extended Data Fig. 4a, right), while the other interface involves Vif residues in the $^{55}VxIPLx_{4–5}L^{64}$ motif (Extended Data Fig. 4a, left) located on the opposite side of the major A3F interface on Vif (Extended Data Fig. 4a, center), indicating a single A3F molecule would not be able to cover all interacting surfaces on Vif simultaneously. The structure shows that the tetramer interfaces are mediated by $A3F_{CTDm}$, consistent with our observation that the Vif–CBFβ subcomplex alone does not form tetramers (Extended Data Fig. 4b, left). We also confirmed that the tetramer was not induced by the solubility-enhancing mutations in $A3F_{CTDm}$, as reverting those located near the tetramer interfaces back to wild type residues did not affect the tetramer formation (Extended Data Fig. 4b, right). However, when we mutated A3F D347 located at one of the tetramer interface (Extended Data Fig. 4a, right) to Arg, the D347R substitution disrupted the tetramer formation but did not affect the formation of the Vif–CBFβ–$A3F_{CTDm\text{-}D347R}$ ternary complex *in vitro* (Extended Data Fig. 4c). Consistently, our functional data showed that the D347R mutant of the full-length A3F behaved the same as WT A3F in terms of its antiviral activity and sensitivity to Vif-mediated degradation, which resulted in rescue of viral infectivity (Extended Data Fig. 4d). These results demonstrate that the major interface observed in the Vif–CBFβ–$A3F_{CTDm}$ ternary complex should represent the primary interaction mode of A3F recruitment to the Vif-containing E3 ligase, and argue against the possible biological significance of the tetramer. However, we cannot rule out the possibility that some of the observed tetramer interface interactions may be involved during the Vif antagonization of A3F.

DISCUSSION

Our structure establishes an unambiguous, comprehensive interaction model, enabling the reevaluation and interpretation of the extensive but sometimes confusing mutagenesis observations [16,20,25–32,36,37]. It allows for the delineation between residues directly

participating in the interactions, and those contributing indirectly by maintaining the conformation required for the interactions. In fact, many of the residues previously speculated to be at the A3F-Vif interface are either buried in the molecular core or serve indirect structural roles at the Vif-CBFβ interface. Moreover, a previous interaction model predicted an electrostatic interaction between Vif R15 and A3F E289 based on genetic and computational analysis [37]. However, these two residues are located far away from each other in our structure (Extended Data Fig. 7a), and Vif_{R15E} mutant failed to restore the degradation and viral infectivity against $A3F_{E289K}$ mutant (Extended Data Fig. 7c), contradictory to the prior charge-swapping mutagenesis result [37]. In contrast, our structural, biochemical, and cellular data unambiguously elucidate the correct interactions at the interfaces between Vif–CBFβ and A3F (Fig 2 and 3). These advances demonstrate the power of the structure in synthesizing and clarifying the existing data to further our understanding of the molecular basis of Vif-mediated degradation of A3F.

Our Vif–CBFβ–$A3F_{CTDm}$ structure not only provides the structural basis of A3F targeting by HIV-1 Vif, but also enables a deeper understanding of Vif interactions with other A3s. Notably, many of the Vif residues proposed to participate in both A3F and A3G interactions based on mutagenesis studies [18] are not found at the Vif-A3F interfaces. As mentioned above, they play indirect structural roles in the Vif core or its interaction with CBFβ, indicating that Vif recruits A3F and A3G through distinct interfaces with considerably less overlapping regions than expected (Fig. 4a). In addition, our structure shed light on a similar Vif interface speculated for A3C, which together with $A3D_{CTD}$, falls into the same A3 zinc domain group as $A3F_{CTD}$ [16,30,38]. Nonetheless, differences exist within the group such as the Vif C-terminal residues E171 and R173, previously found to be less critical for the degradation of A3C [27], are important for A3F interaction. Our work also substantiates the prediction that A3F uses a surface opposite from that of A3G to interact with Vif [39–45], while A3F and A3C contact Vif using similar regions [16,27,30]. These comparisons show that Vif is a versatile A3 binder, targeting a variety of A3s with regions of various degrees of overlap.

Our Vif–CBFβ–$A3F_{CTDm}$ structure also provide insights into the potential degradation-independent mechanisms of Vif-mediated inhibitions on A3s. The ternary structure shows that $A3F_{CTDm}$ contacts Vif/CBFβ through an interface away from its catalytic site (Figs. 1b and 4a), indicating that this interaction should not block the A3F deamination activity. However, our ssDNA deamination assay showed that the catalytic activity of $A3F_{CTDm}$ at low concentration (5 μM) was not affected by two-fold excess of the Vif–CBFβ–EloB–EloC subcomplex, but was inhibited by a large excess (40-fold) of the subcomplex (Extended Data Fig. 8a). This inhibition was not revoked by the Vif R15E mutation (Extended Data Fig. 8a) that disrupted the Vif-$A3F_{CTDm}$ major interface and the Vif-A3F interaction both *in vitro* and *in vivo* (Fig. 3c, Extended Data Fig. 7c). In contrast, at high $A3F_{CTDm}$ concentration (75 μM), two-fold excess of either Vif WT or R15E variants was sufficient to inhibit the $A3F_{CTDm}$ deamination activity (Extended Data Fig. 8a), potentially due to the formation of a higher oligomer state at the high concentration (Extended Data Fig. 1a). These results indicate that interactions other than those at the major interface were involved in the inhibition of the A3F deamination activity. Interestingly, one of the tetramer interfaces observed in our structure involving the Vif $^{55}VxIPLx_{4–5}L^{64}$ motif does have the potential to

block the A3F catalytic site for DNA substrate access (Extended Data Fig. 8b). Even though tetramer formation may not necessarily occur in cells, this observed interface points to the propensity for such an interaction at very high (local) protein concentration leading to inhibition. Several enzymatic studies have also shown that Vif can directly attenuate the deaminase activities of A3G without inducing its proteasomal degradation [46,47], primarily by disrupting the A3G interactions with viral ssDNA, whose binding site is postulated to be adjacent to the major Vif-binding interface in $A3G_{NTD}$ (Fig. 4a, top right). These findings emphasize that Vif antagonizes A3s through multifarious mechanisms regulated by their specific interactions. Further elucidation of the degradation-independent inhibition mechanisms must await future studies.

The work described herein establishes a detailed biochemical and structural framework of how A3F is targeted by HIV-1 Vif and its cellular cofactor CBFβ. This, together with the previous Vif-E3 ligase structure [23], allows a complete mechanistic understanding of Vif-mediated recruitment of A3F to the ubiquitin-proteasome degradation pathway (Fig. 4b). The E2 ubiquitin-conjugating enzyme bound to the flexible Rbx2 component in the NEDD8 activated E3 ligase [48] potentially allows ubiquitination of multiple positions on A3F, as well as the bound Vif molecule [49]. This advance provides critical insights into the molecular interactions enabling the viral evasion of a major host defense, which is also conserved between other known lentiviruses and their hosts [50]. Furthermore, it has been found that HIV-1 can evade A3G, but not A3F restriction in the absence of Vif [51,52], highlighting that the Vif-A3F interaction is essential for HIV-1 survival in cells. Therefore the structural details obtained in this work can effectively facilitate the development of novel anti-HIV therapeutics by specifically targeting the interfaces between Vif–CBFβ and A3F.

ONLINE METHODS

Plasmid construction

HIV-1 Vif residues 1–176 (Vif176) from pNL4–3 and Vif176 with the α-domain (residues 114–157) replaced with a six amino-acid (a.a.) linker (EASEGS) (Vif176Δ114–157) were cloned into the pETDuet vector. 6×His tagged human CBFβ residues 1–187 (CBFβ187) and C-terminal truncated CBFβ residues 1–151 (CBFβ151) were cloned into pCDFDuet vector. MBP-tagged EloB residues 1–118 (EloB118) and 6×His tagged EloC residues 17–112 (EloC17–112) were cloned into the pACYCDuet vector. 6×His tagged human A3F residues 185–373 with ten solubility mutations (Y196D, H247G, C248R, F302K, W310K, Y314A, Q315A, K355D, K358D, and F363D) [24], which has been thoroughly validated to retain wild type-like deamination activities, Vif responsiveness, and structure, termed as $A3F_{CTDm}$ in this study (the other $A3F_{CTDm}$ variants were constructed on this background) was fused to CBFβ151 or CBFβ187 through a 40 a.a. linker (GVDGSDEASELACPTPKEDGLAQQQTQLNLRSQATGSGSG) to stabilize Vif binding. Each of the $A3F_{CTDm}$-CBFβ fusion protein variants or the 6×His tagged $A3F_{CTDm}$ alone was cloned into the pCDFDuet vector. An A3G chimera was created in which a modified rhesus $A3G_{NTD}$ [53] was fused to human $A3G_{CTD}$, with a K128D mutation to enable binding to HIV-1 Vif. This chimera (referred to as $A3G_{rh\text{-}hu}$ in this study) showed a solution property superior to that of wild-type human A3G and was used in the *in vitro* binding assays. The

6×His tagged $A3G_{rh\text{-}hu}$ was cloned into the pETDuet vector. All Duet vectors were from Novagen, Inc. All mutants were constructed following the protocol of QuikChange II Site-Directed Mutagenesis Kit (Agilent Technologies).

For the cell-based assays, the following previously described plasmids or their derivative mutants were used, including, pFlag-CBFβ, pFlag-A3F, pFlag-A3G, pVif-HA, pHDV-eGFP, and pHCMV-G, which expresses vesicular stomatitis virus glycoprotein (VSV-G) [16,20,54–58]. Vif, CBFβ, and A3F mutants were generated by site-directed mutagenesis using a QuickChange Lightening Multi Site-directed mutagenesis kit (Agilent Technologies) and verified by sequencing.

Protein expression and purification

The *Escherichia coli* BL21 (DE3) cells (New England BioLabs) were used for protein expressions. Vif176 and 6×His tagged $A3F_{CTDm}$-40-CBFβ187 constructs were co-expressed to obtain the Vif–CBFβ–$A3F_{CTDm}$ complex. Vif176Δ114–157 and 6×His tagged $A3F_{CTDm}$-40-CBFβ151 constructs were co-expressed to obtain the truncated Vif–CBFβ–$A3F_{CTDm}$ complex. In addition, the truncated Vif176Δ114–157 and 6×His tagged CBFβ151 constructs were co-expressed, and 6×His tagged $A3F_{CTDm}$ was separately expressed to reconstitute the unfused Vif–CBFβ–$A3F_{CTDm}$ complex. Vif176 variants, 6×His tagged CBFβ187 variants, MBP-tagged EloB118/EloC were co-expressed to form various MBP-tagged Vif–CBFβ–EloB–EloC variants, while the 6×His tagged $A3F_{CTDm}$ variants, 6×His tagged CBFβ187, 6×His tagged $A3G_{rh\text{-}hu}$ were separately expressed for *in vitro* binding assays. The protein expression was induced by 0.3 mM isopropyl β-D-1-thiogalactopyranoside (IPTG) at 16 °C for 16 hours in Terrific Broth.

Cells were harvested and lysed by a microfluidizer. The lysate was clarified by centrifugation and then applied to a Ni-NTA (Qiagen) column. The fused Vif–CBFβ–$A3F_{CTDm}$ complexes or the Vif–CBFβ subcomplexes were then purified by two rounds of size exclusion chromatography (SEC) (HiLoad Superdex 200, GE healthcare), first in a buffer containing 30 mM Tris, 1 M NaCl, 0.2 mM TCEP, pH 8.0 to remove bound nucleic acids, and followed by a second SEC run at a low salt of 80 mM NaCl. The purification of all other proteins were performed following the Ni-NTA step by anion exchange (HiTrap Q HP, GE healthcare) chromatography in a buffer of 30 mM Tris, 0.2 mM TCEP, pH 8.0 with a gradient NaCl concentration from 20 mM to 1M, and subsequently SEC (HiLoad Superdex 200 or 75, GE healthcare) in a buffer of 30 mM Tris, 300 mM NaCl, 0.2 mM TCEP, pH 8.0 ($A3G_{rh\text{-}hu}$ in 1M NaCl). Purity of the proteins was analyzed by SDS-PAGE after each step.

Binding assays of Vif–CBFβ–$A3F_{CTDm}$ complexes *in vitro*

SEC binding assay: Various amounts of the truncated Vif–CBFβ subcomplex were incubated with $A3F_{CTDm}$ at 1:1 molar ratio in the buffer of 30 mM Tris, 100 mM NaCl, 0.2 mM TCEP, pH 8.0 at 4 °C for 2 hours; the ternary complex formation was then analyzed by SEC (Superdex 200). Similarly, high amount of CBFβ and $A3F_{CTDm}$ were incubated at 1:1 molar ratio in the same buffer at 4 °C for 6 hours. The retention volumes of individual CBFβ, $A3F_{CTDm,}$ and their mixture at equal concentrations were analyzed by SEC (Superdex 75), and the peak fractions of all three species were analyzed by SDS-PAGE. The Vif–CBFβ–

Cul5 E3 ligase complex was formed by incubating the Vif–CBFβ–EloB–EloC complex and Cul5–Rbx2 complex with 1:1 molar ratio at 4°C for 2 hours and further purified by SEC (Superdex 200).

Pull-down assay: 0.15 mg of MBP-tagged Vif–CBFβ–EloB–EloC variants were first incubated with $A3F_{CTDm}$ variants or $A3G_{rh\text{-}hu}$ at 1:2 molar ratio in 100 μl binding buffer containing 30 mM Tris, 100 mM NaCl, 0.2 mM TCEP, pH 8.0 at 4 °C for 2 hours, subsequently mixed with 50 μl of amylose resin (New England BioLabs) in a Pierce spin column (Thermo Fisher) and incubated for one additional hour. After removing the supernatant by centrifugation, the resin was washed with 300 μl of binding buffer for three times. 80 μl of the elution buffer (binding buffer plus 0.2 mM maltose) was then added to the resin and incubated at 4 °C for 10 minutes before centrifugation. The loading and elution fractions were analyzed by SDS-PAGE.

A3 degradation assays, virus production, and determination of infectivity

TZM-bl and 293T cells were maintained in Dulbecco's modified Eagle's medium (DMEM) (Corning Cellgro) containing 10% fetal bovine serum (Hyclone), and 1% penicillin-streptomycin (GIBCO). To produce virus, 293T cells were seeded at 4×10^5 cells/well in six-well plates and co-transfected using Lipofectamine2000 (Invitrogen) with the following plasmids: pHDV-eGFP (2 μg), phCMV-G (200 ng), WT or mutant pFlag-A3F (250 ng) or pFlag-A3G (500 ng), and WT or mutant pVif-HA (2.5 μg). After 48 hours, the virus-containing supernatants were filtered through 0.45-μm filter and kept at −80 °C until use. Producer cell lysates were also harvested for immunoblotting analyses to detect the steady-state levels of A3F and A3G in the absence or presence of Vif. Flag-A3F and Flag-A3G were detected using a rabbit anti-Flag polyclonal antibody or a mouse monoclonal anti-Flag antibody (Sigma; both at a 1:5000 dilution). CBFβ was detected using a rabbit anti-CBFβ polyclonal antibody (Abcam), a mouse monoclonal anti-Flag antibody, or a rabbit anti-myc polyclonal antibody (Sigma; all of them used at a 1:5000 dilution), Vif was detected using a mouse anti-HA monoclonal antibody (Sigma) or a rabbit monoclonal anti-HA antibody (Cell Signaling); both at 1;5000 dilution, and HSP90 was detected using mouse anti-HSP90 antibody (Santa Cruz Biotechnology; at 1:20000 dilution). Rabbit and mouse primary antibodies were detected using an IRDye® 800CW-labeled goat anti-rabbit secondary antibody at 1:5000 dilution (Licor) or an IRDye® 680-labeled goat anti-mouse secondary antibody at 1:5000 dilution (Licor). Protein bands were visualized and quantified using Odyssey® Infrared Imaging System and Image Studio™ Lite version (Licor).

To determine infectivity, virus stocks were quantified using a p24 CA enzyme-linked immunosorbent assay (XpressBio) and TZM-bl luciferase reporter assay was performed as previously described [59].

CBFβ knockdown and back complementation with CBFβ mutants

To knockdown endogenous CBFβ and complement with exogenous CBFβ variants, 293T cells were seeded at 2.5×10^5 cells per well in six-well plates a day before transfection. Next day, cells were transfected using Lipofectamine RNAiMAX (Invitrogen) with Stealth CBFβ siRNA targeting 3-UTR region (Invitrogen; NM_022845.2_stealth_865) as previously

described [59]. Next day, using the Lipofectamine2000 transfection method (Invitrogen), the following plasmids were co-transfected: pHDV-eGFP (2 μg), phCMV-G (200 ng), Flag-CBFβ variants (500 ng), and Vif (2.5 μg) in combination with the CBFβ siRNA and pFlag-A3F (250 ng) or pFlag-A3G (500 ng). Producer cell lysates and supernatants were collected 48 hours later for western blotting and infectivity assays, respectively.

Co-immunoprecipitation assays

Flag Co-IP assays were carried out as previously described [59]. Briefly, 293T cells were seeded at 4×10^6 cells per 10-cm dish and transfected the next day using standard methods. The following DNA amounts were used to transfect 293T cells: 4 μg Flag-A3F, 4 μg CBFβ-myc, and 2 μg Vif-HA expression plasmids. Next day, the cells were treated with MLN-4924 (BioVision; Cat # 2566) at 2 μM final concentration for 24 hours to prevent Vif-mediated proteasomal degradation of A3F. 48 hours post-transfection, total cell lysates were harvested in 1 mL of RIPA lysis buffer (Sigma) supplemented with proteinase cocktail inhibitors EDTA-free tablets (Roche) with or without benzonase® nuclease (250U/ml final concentration; Sigma) addition and Flag Co-IP was performed at 4°C for overnight. To detect eluted complexes as well as the input cell lysates, western blotting was performed. CBFβ was detected using a rabbit anti-myc polyclonal antibody at a 1:5000 dilution, Vif was detected using a rabbit anti-HA monoclonal antibody at a 1:5000 dilution, and A3F detected using a mouse anti-Flag antibody at a 1:5000 dilution. HSP90 was used as loading control and detected with mouse anti-HSP90 antibody at a 1:20000 dilution. Protein bands were visualized using an Odyssey® Infrared Imaging System (Licor) as described above.

UDG-based deamination assay

Various amounts (5 μM or 75 μM) of 6×His tagged $A3F_{CTDm}$ was incubated with MBP-tagged Vif–CBFβ–EloB–EloC at 1:2 or 1:40 molar ratio in 10 μl buffer of 30 mM Tris pH 7.10, 50 mM NaCl, 1mM $MgCl_2$, 5% glycerol, 0.5 mM EDTA and 0.2 mM TCEP at 4°C for 2 hours, followed by the addition of 5 μM of 6-FAM labeled ssDNA oligo substrate containing a T<u>C</u> hotspot (5'-TAAGAAAGAATTCAGAAGAGGAA-3'). The reaction mixtures were then incubated at room temperature for overnight (for 5 μM $A3F_{CTDm}$) or 3 hrs (for 75 μM $A3F_{CTDm}$) and terminated at 95°C for 5 minutes. 5 units of uracil DNA glycosylase (UDG, New England BioLabs) were added into the reactions for incubation at 37°C for 1 hour, and then treated with 0.25 M NaOH at 37°C for 30 minutes. 10 μL of 1 M Tris pH 8.0 was then added to neutralize the pH of the samples and equal volume of formamide was added to the samples as loading buffer. The samples were analyzed on a 15% TBE-Urea gel (Invitrogen), which was imaged on a BioRad ChemiDoc.

Cryo-EM sample preparation, data collection and processing

Purified protein complex (4 μl) was applied to a C-Flat 2/1 3C copper grid (Electron Microscopy Sciences) pretreated by glow-discharging at 8 mA for 20 seconds. The grid was blotted at 10 °C with 100% humidity and plunge-frozen in liquid ethane using FEI Vitrobot Mark IV (Thermo Fisher). The grids were stored in liquid nitrogen before data collection.

Images were acquired on a FEI Titan Krios electron microscope (Thermo Fisher) equipped with Gatan K2 Summit direct detector in super-resolution mode, at a calibrated

magnification of 130,000× with the physical pixel size corresponding to 1.05Å. Detailed data collection statistics for the Vif–CBFβ–A3F$_{CTDm}$ complexes have been indicated in Table 1. Automated data collection was performed using SerialEM [60].

A total of 3486 movie series without tilting the microscope stage and a total of 3359 movie series with the stage tilted by −30° were collected for the truncated Vif–CBFβ–A3F$_{CTDm}$ complex, and a total of 2768 movie series with the stage tilted by −30° were collected for the Vif–CBFβ–A3F$_{CTDm}$ complex. Tilting the stage helped alleviate modest preferred orientation problem of the samples. The same data processing procedures were carried out for each complex described as below. Motion correction of each micrograph was determined using MotionCor2 [61] and contrast transfer function (CTF) estimation was calculated using Gctf [62]. Around 5000 particles were manually picked from selected micrographs to generate initial 2D class averages by RELION [63] as the templates for automatic particle picking of the entire dataset by Gautomatch (https://www.mrc-lmb.cam.ac.uk/kzhang/). All particles were included directly for 3D classification in RELION to include those at rare views that may not have sufficient numbers to generate good 2D classes. For the Vif–CBFβ–A3F$_{CTDm}$ complex, the 3D classification without imposing symmetry produced one good 3D class out of fifteen, containing 165629 particles. Conformational flexibility was detected in 3D classes (Extended Data Fig. 2c). The good 3D class was used for gold standard refinement in RELION with D2 symmetry. The final resolution of the reconstruction was 5.0 Å, based on the Fourier shell correlation (FSC) cutoff at 0.143 between the two half maps [64], after a soft mask was applied to mask out solvent region (Extended Data Fig. 9a). The final map was corrected for K2 detector modulation and sharpened by a negative *B*-factor within RELION [65]. Particles of the truncated Vif–CBFβ–A3F$_{CTDm}$ complex was processed in a similar way. The truncated complex showed less conformational flexibility and obeyed the D2 symmetry better (Extended Data Fig. 2c). A good 3D class of 337256 particles was identified after combining 1243243 titled and 1197365 untilted particles. The particles showed some orientation preferences (Extended Data Fig. 9b), which resulted in a final reconstruction of 3.9 Å resolution (Extended Data Fig. 9a). Local resolution variation was estimated by using RELION (Extended Data Fig. 9c).

Model building and refinement

The structures of the Vif–CBFβ portion (extracted from PDB 4N9F) and A3F$_{CTD}$ (PDB 3WUS) were docked into the cryo-EM maps of the truncated and full Vif–CBFβ–A3F$_{CTDm}$ complex using Chimera [66] and refined with *phenix.real_space_refine* module in PHENIX with secondary structure restraints and Ramachandran restraints [67]. The model of the truncated Vif–CBFβ–A3F$_{CTDm}$ complex was further adjusted in COOT [68] manually with intervening cycles of refinement in PHENIX and Refmac5 [69]. The final model with good geometry and fit to the map was validated using the comprehensive cryo-EM validation tool implemented in PHENIX [70] (Table 1). All structural figures were generated using PyMol [71] and Chimera [66].

Reporting Summary

Further information on experimental design is available in the Nature Research Reporting Summary linked to this article.

Data Availability

The model of the truncated Vif–CBFβ–A3F$_{CTDm}$ complex has been deposited in the wwPDB with accession code PDB 6NIL. The cryo-EM maps of the truncated and full-length Vif–CBFβ–A3F$_{CTDm}$ complexes have been deposited in EMDB with accession codes EMD-9380 and EMD-9381, respectively. Source data for Fig. 2c,d,e, Fig. 3c,d,e,f,g, Extended Data Fig. 1b,c, Extended Data Fig. 4c,d, Extended Data Fig. 5b,c, Extended Data Fig. 6a,b, and Extended Data Fig. 7b,c are available with the paper online. Other data are available from corresponding authors upon reasonable request.

Extended Data

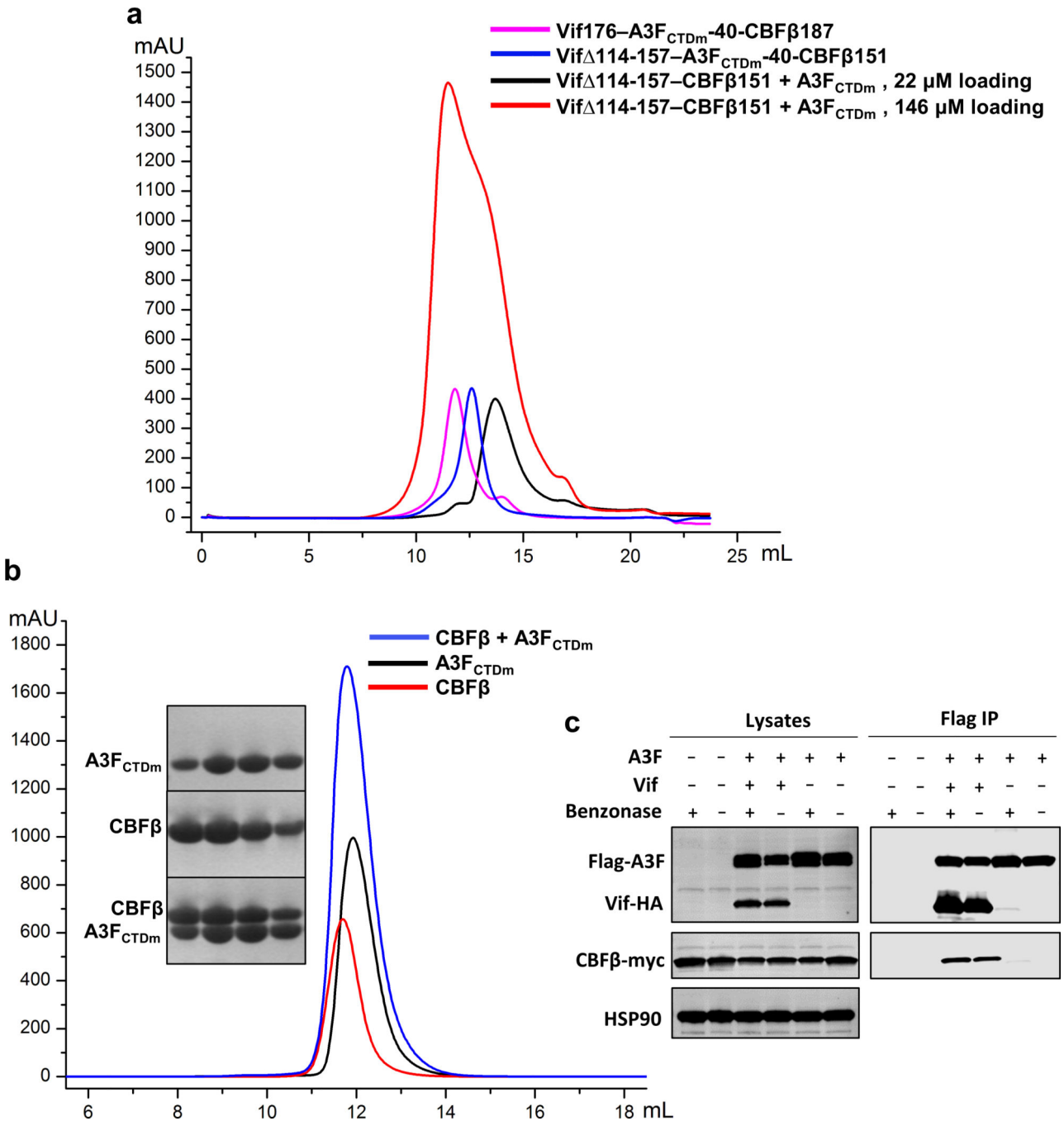

Extended Data Fig. 1. Biochemical and cellular characterizations of various Vif–CBFβ–A3F$_{CTDm}$ assemblies and the A3F$_{CTDm}$-CBFβ interaction.

a, The Vif–CBFβ–A3F$_{CTDm}$ fusion complex with or without the Vif α-domain and corresponding interacting CBFβ C-terminus stays as tetramer in low salt solution. The unfused Vif–CBFβ–A3F$_{CTDm}$ without these regions switches from monomer to tetramer at high protein concentration (146 μM loading concentration). **b**, No obvious shift for the elution peak was observed upon incubation of CBFβ and A3F$_{CTDm}$ compared to the CBFβ alone or A3F$_{CTDm}$ alone. The SDS-PAGE analysis of the peak fractions of CBFβ alone,

$A3F_{CTDm}$ alone and CBFβ/$A3F_{CTDm}$ mixture is indicated. **c**, Co-immunoprecipitation (Co-IP) analysis of the interaction between A3F and CBFβ in the presence or absence of Vif in cells. Flag-A3F and CBFβ-myc were co-transfected with or without Vif-HA and co-immunoprecipitated using anti-Flag antibody. In the absence of Vif, no binary A3F and CBFβ binding was observed. A representative blot from two independent experiments was shown.

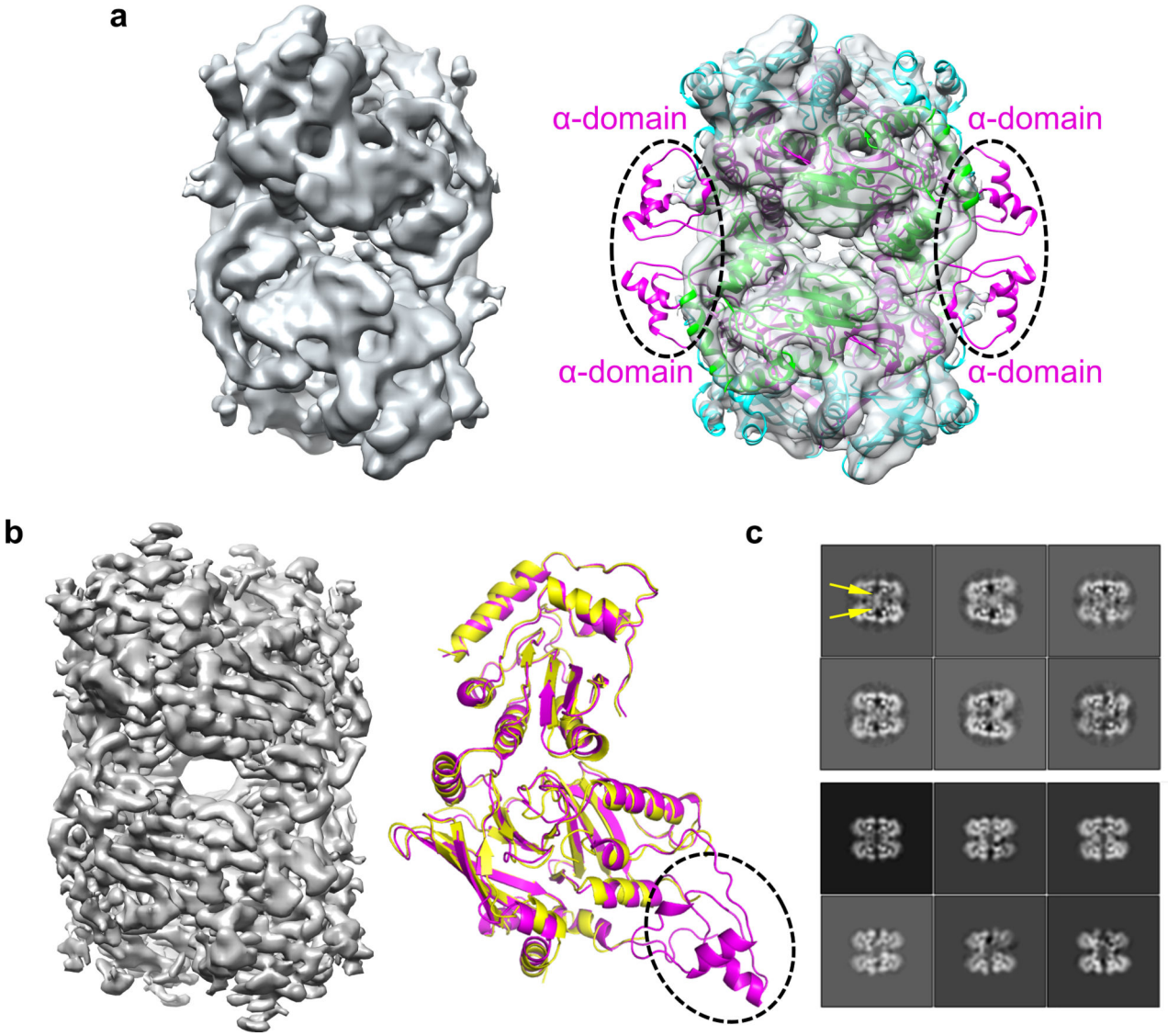

Extended Data Fig. 2. Cryo-EM study of the Vif–CBFβ–A3F$_{CTDm}$ complex with or without the Vif α-domain and the corresponding interacting region of the CBFβ C-terminus.

a, The 5 Å cryo-EM reconstruction of Vif–CBFβ–A3F$_{CTDm}$ with (right) or without (left) the docked-in model (ribbon). The density corresponding to the flexible Vif α-domain and the corresponding interacting CBFβ C-terminus (circled) is not visible. **b**, Left, the 3.9 Å cryo-EM reconstruction of the truncated Vif–CBFβ–A3F$_{CTDm.}$ Right, overlay of the cryo-EM models of Vif–CBFβ–A3F$_{CTDm}$ ternary complexes with (magenta) and without (yellow) the Vif α-domain and the corresponding interacting CBFβ C-terminus shows that the removal of these regions does not affect the architecture of the ternary complex. **c**, Central slices of the top 3D classes of the Vif–CBFβ–A3F$_{CTDm}$ complex with (upper) or without (lower) the Vif α-domain and the corresponding interacting CBFβ C-terminus indicate that removing these flexible regions reduces the tetramer flexibility. The location of the Vif α-domain and the corresponding interacting CBFβ C-terminus is marked by yellow arrows in the first class average.

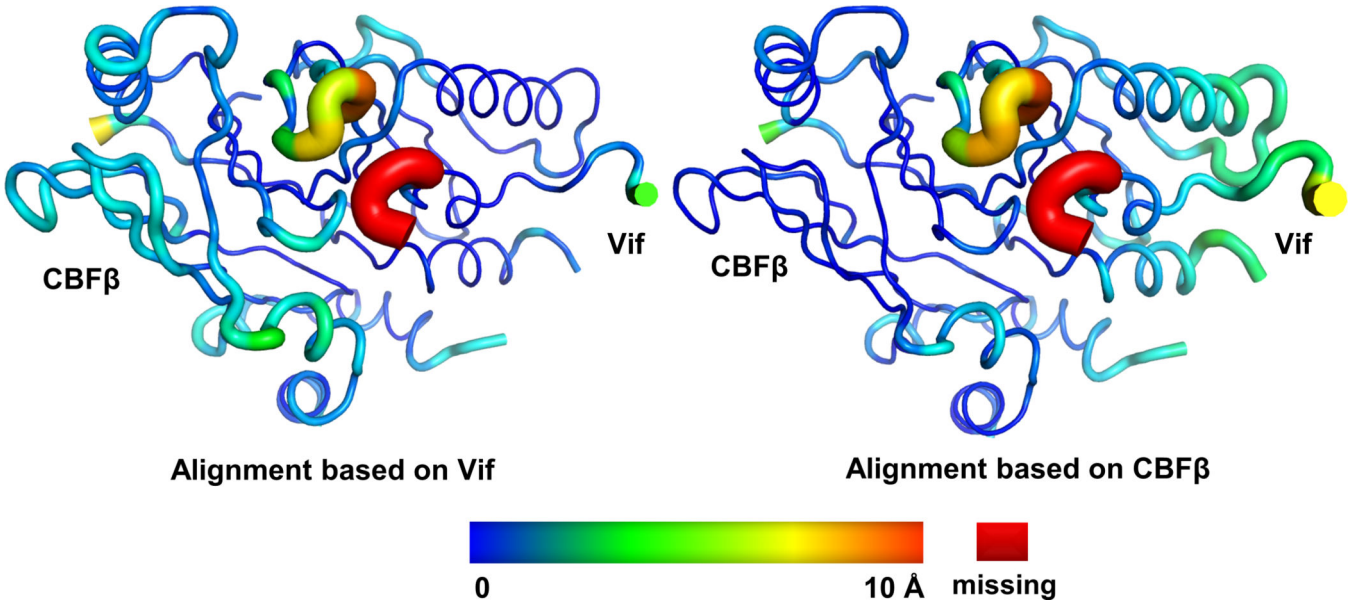

Extended Data Fig. 3. The relative conformational changes between Vif and CBFβ upon $A3F_{CTDm}$ binding, shown as rainbow putty representations of superpositions.

The color spectrum and the coil thickness represent the deviation of the aligned Cα atoms in the structures, which varies from 0 Å (blue) to ~10 Å (orange). The Vif C-terminal residues 173–176 missing in the Vif–E3 ligase structure are colored in red. The Vif–CBFβ structure without $A3F_{CTDm}$ binding used for superposition is extracted from the Vif–E3 ligase structure (PDB 4N9F).

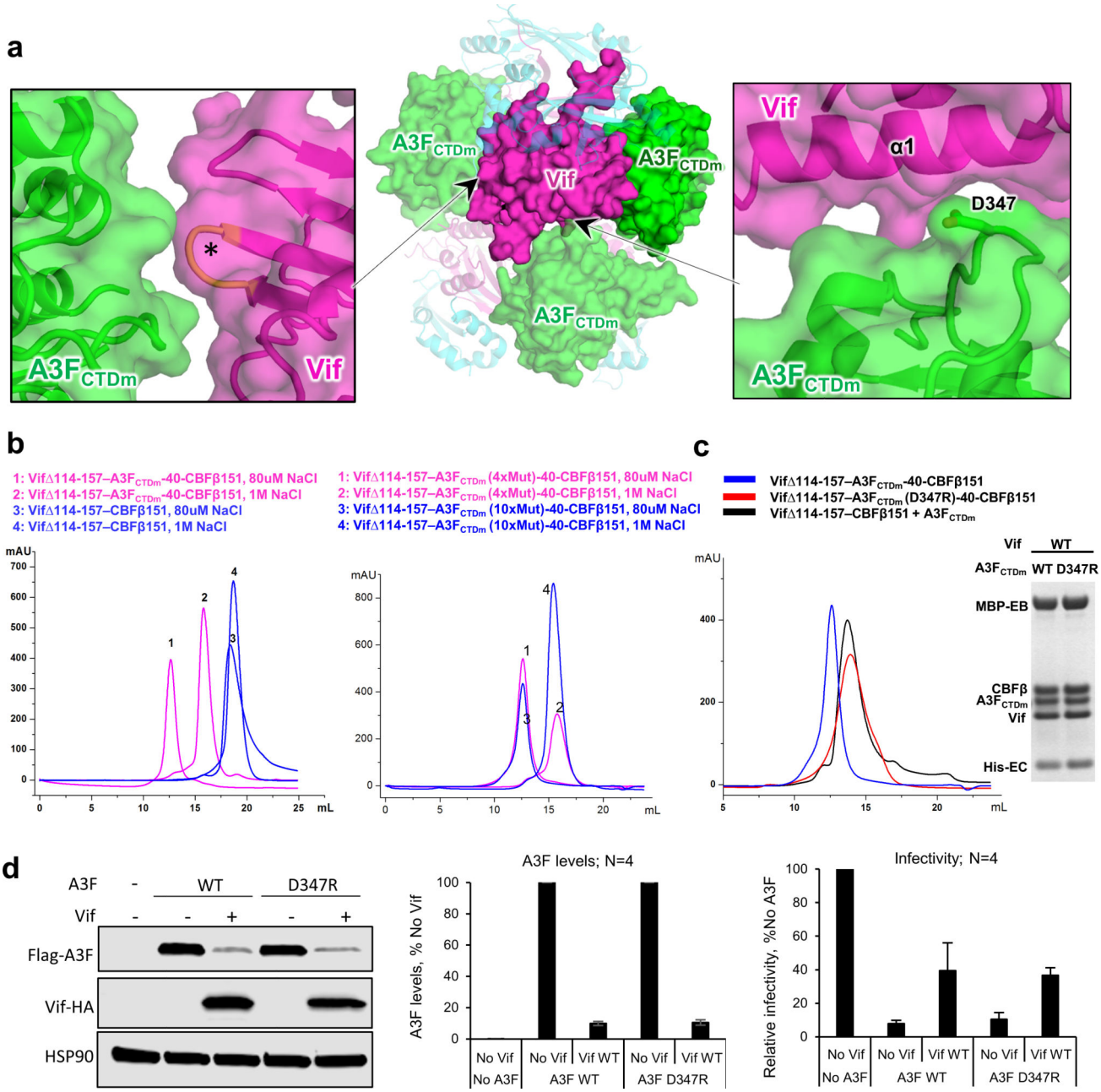

Extended Data Fig. 4. Effects of Vif–CBFβ–A3F$_{CTDm}$ tetramer on A3F-Vif interaction, Vif-mediated A3F degradation, and viral infectivity.

a, Inter-ternary complex interfaces between Vif and A3F$_{CTDm}$ detected in the tetrameric complex. Center, Overview of the two inter-ternary complex interfaces (pointed to by the arrows) involving one Vif molecule. Vif is shown in magenta, CBFβ in cyan, and A3F$_{CTDm}$ in green. One ternary complex containing the major Vif-A3F interface is marked by an oval. The detailed illustrations of the two interfaces are shown on the sides, with one involving the Vif α1 helix (right), and the other involves Vif residues (orange, marked by *) in the 55VxIPLx4–5L64 motif (left). **b,** SEC binding assays show that the tetramer formation depends on the presence of A3F$_{CTDm}$ (left) but not on the solubility-enhancing mutations of

$A3F_{CTDm}$ (right). In contrast to the Vif–CBFβ–$A3F_{CTDm}$ complex which switched from monomer to tetramer when reducing salt concentration, Vif-CBFβ alone stayed as monomer. Six $A3F_{CTDm}$ residues (196, 247, 248, 310, 314, 315) located near the observed tetramer interfaces were reverted back to WT amino acids to verify that this $A3F_{CTDm}$ variant (with 4 remaining point mutations away from the interface and without any disturbance to A3F structure) retained the ability to form tetramers. **c,** SEC binding (left) and MBP pull-down (right) assays show that the $A3F_{CTDm}$ D347R mutation disrupts the tetramer formation but not the individual Vif–CBFβ–$A3F_{CTDm}$ ternary complex. The loading controls are shown in Supplementary Fig. 1b & c. **d,** The effect of D347R mutation on A3F sensitivity to Vif-mediated degradation indicated by western blot (left), quantified A3F levels relative to No Vif (mean ± s.d.; n=4 biologically independent experiments; middle), and relative infectivity (mean ± s.d.; n=4 biologically independent experiments; right). $A3F_{D347R}$ retained WT A3F-like sensitivity to Vif-mediated degradation, which resulted in rescue of viral infectivity.

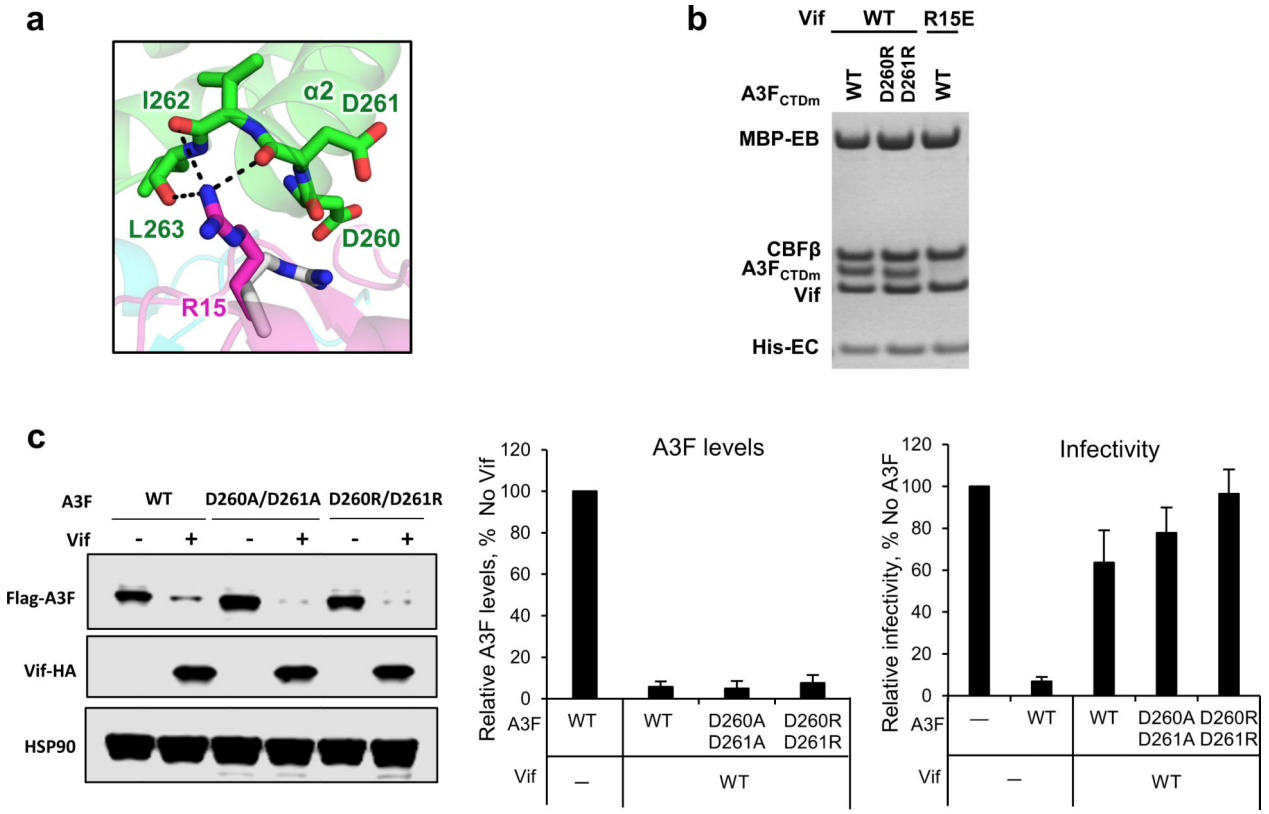

Extended Data Fig. 5. Vif R15 is located at the C-terminus of A3F$_{CTDm}$ α2 helix interacting with the backbone carbonyls of the helix.

a, Upon A3F binding, Vif R15 flips away from the position (gray) pointing into the molecule core to electrostatically interact with the backbone carbonyls of A3F$_{CTDm}$ α2 helix rather than the side chain carboxylates of D260/D261. **b**, Mutational analysis of the interactions by *in vitro* binding assay using MBP-tagged Vif–CBFβ–EloB–EloC variants to pulldown A3F$_{CTDm}$ variants. The D260R/D261R double mutation did not affect the Vif interaction. The loading controls are shown in Supplementary Fig. 1b & c. **c**, The effect of D260A/D261A or D260R/D261R double mutants on A3F sensitivity to Vif-mediated degradation indicated by western blot (left), quantified A3F levels relative to No Vif (mean ± s.d.; n=3 biologically independent experiments; middle), and relative infectivity (mean ± s.d.; n=3 biologically independent experiments; right). Both alanine and arginine mutants did not confer resistance, indicating that the side chains of the residues are not involved in the Vif interaction.

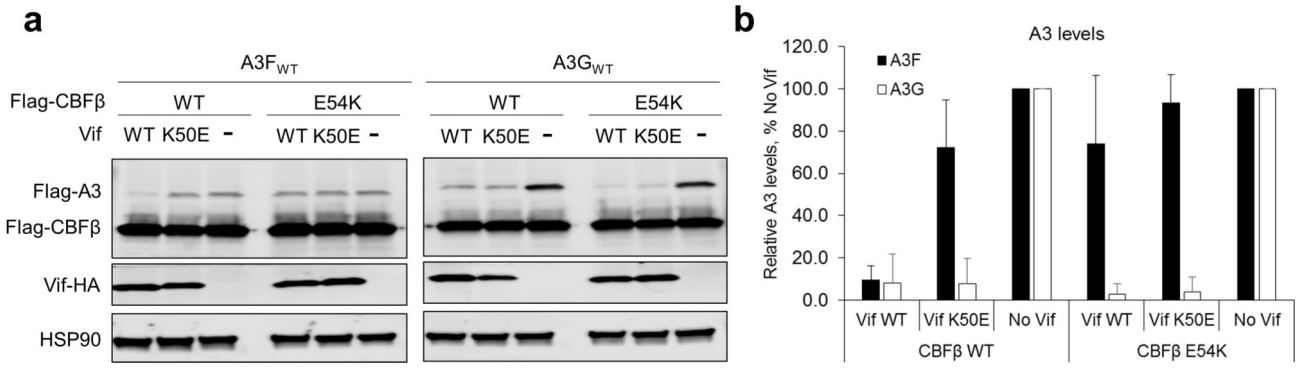

Extended Data Fig. 6. Analysis of the effect of Vif K50E mutation on A3G degradation in cells.

Western blot (**a**) and quantified A3 levels relative to No Vif (**b**) show that the Vif K50E mutant could not induce A3F degradation in the presence of either CBFβ WT or CBFβ E54K but could induce A3G degradation (mean ± s.d.; n=3 biologically independent experiments).

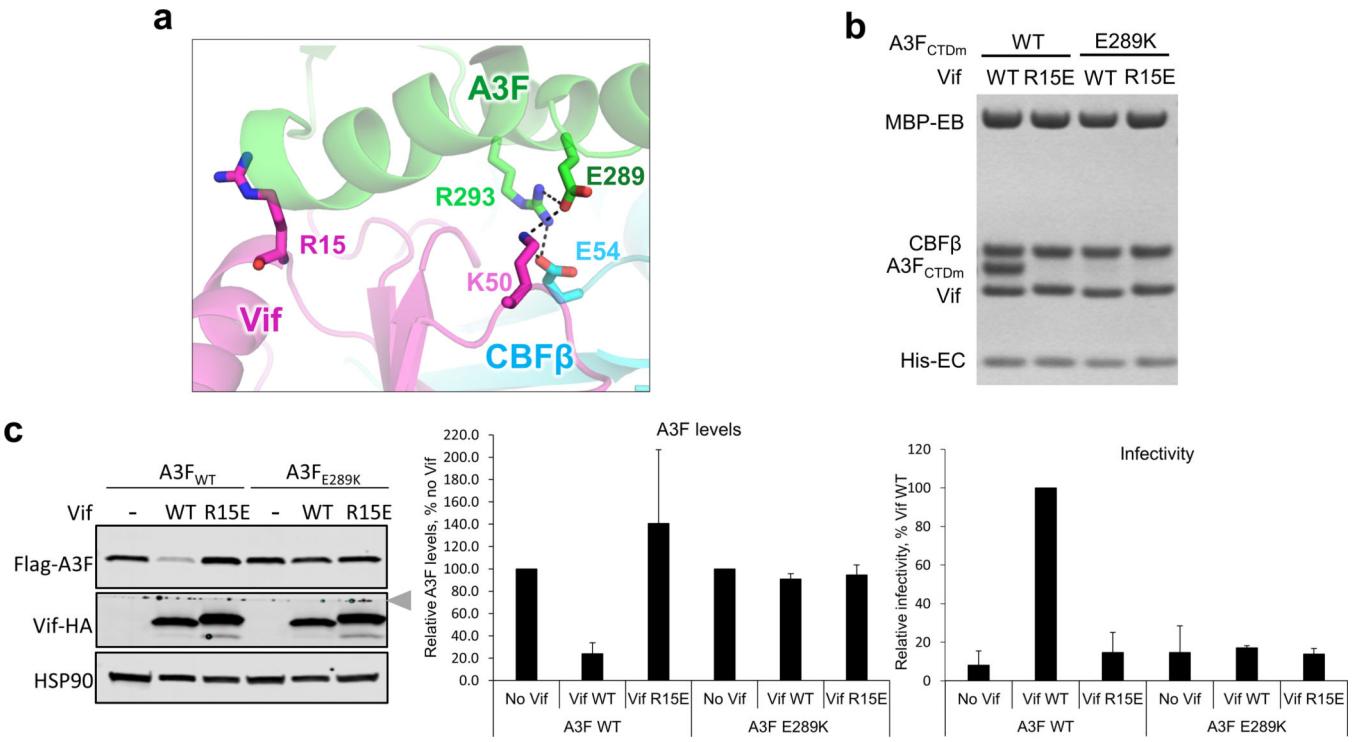

Extended Data Fig. 7. HIV1-Vif R15 does not interact with A3F E289.

a, Vif R15 is located far away from A3F E289, which interacts with Vif K50 in the Vif–CBFβ–A3F$_{CTDm}$ structure. **b**, Mutational analysis of the interactions by *in vitro* binding assay using MBP-tagged Vif–CBFβ–EloB–EloC variants to pulldown A3F$_{CTDm}$ variants. The loading controls are shown in Supplementary Fig. 1b & c. The charge-swapped Vif R15E/A3F E289K double mutation did not rescue the Vif-A3F interaction *in vitro*. **c**, The effect of Vif R15E or A3F E289K mutation on A3F sensitivity to Vif-mediated degradation indicated by western blot (left), quantified A3F levels relative to No Vif (mean ± s.d.; n=3 biologically independent experiments; middle), and relative viral infectivity (mean ± s.d.; n=3 biologically independent experiments; right). In contrast to the prior report [37], the charge-swapped Vif R15E/A3F E289K double mutation did not restore the Vif-mediated A3F degradation or viral infectivity in cells. The blot was cut as indicated (gray arrow), where one half was used to detect Flag-A3F and HSP90, and the other half was used to detect Vif-HA.

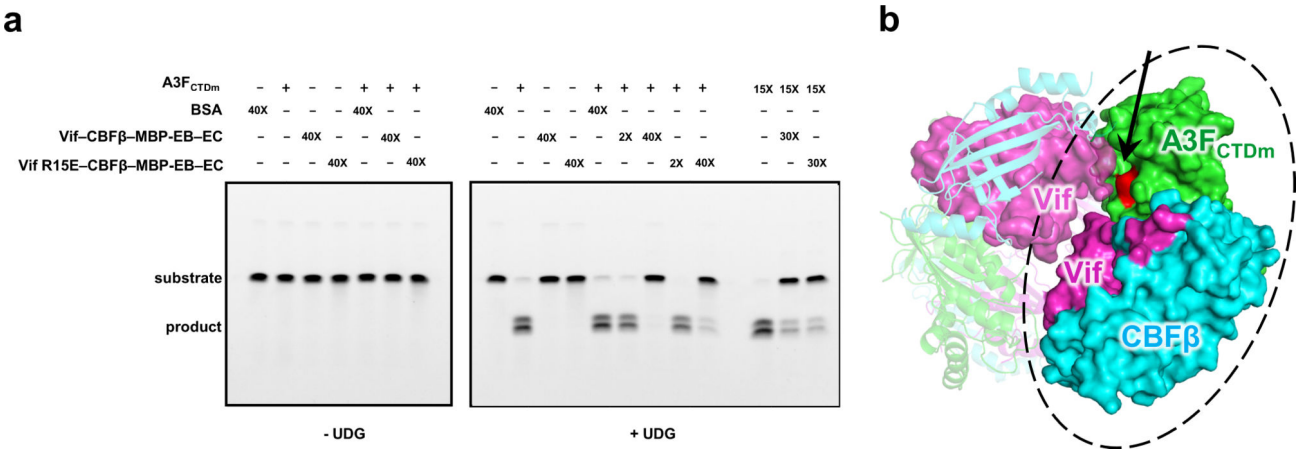

Extended Data Fig. 8. Effect of Vif–CBFβ–A3F$_{CTDm}$ complex on A3F$_{CTDm}$ deaminase activity.

a, UDG-based deamination assay of A3F$_{CTDm}$ (+: 5 μM; 15×: 75 μM) in the presence or absence of different molar excesses (2×: 10 μM; 30×: 150 μM; 40×: 200 μM) of Vif–CBFβ–EloB–EloC variants. The inhibition of A3F$_{CTDm}$ deamination activity by a large excess of Vif–CBFβ–EloB–EloC variants was not caused by nonspecific binding interactions as the same molar amount excess (40×) of BSA did not trigger the inhibition.

b, One of the Vif–CBFβ–A3F$_{CTDm}$ tetramer interface involving the ^{55}VxIPLx$_{4–5}$L^{64} motif (Extended Data Fig. 4a, left) blocks the catalytic site of A3F$_{CTDm}$ (red and marked by an arrow). Vif is shown in magenta, CBFβ in cyan, and A3F$_{CTDm}$ in green. One Vif–CBFβ–A3F$_{CTDm}$ ternary complex with the major interface is circled with an oval.

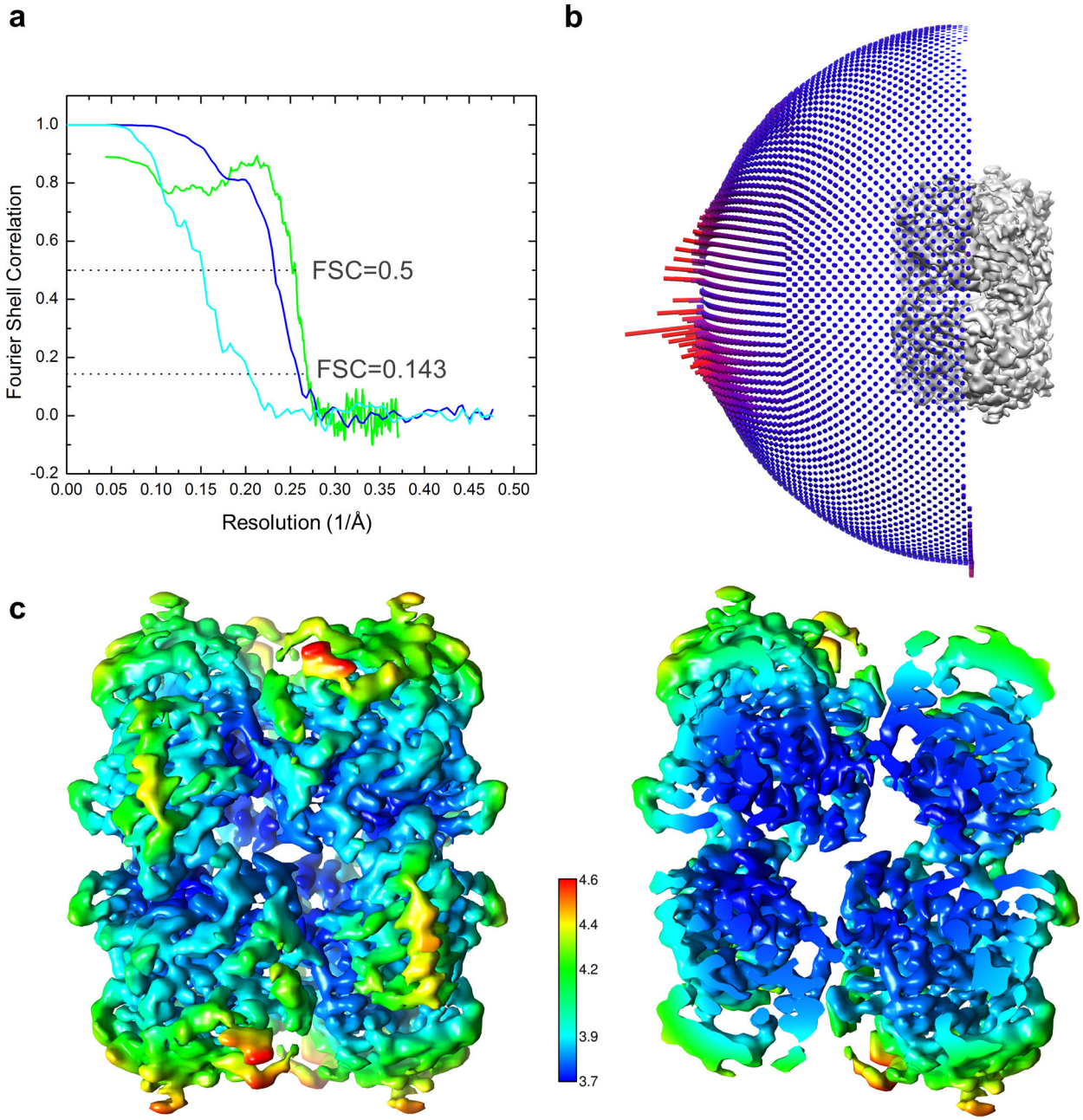

Extended Data Fig. 9. Parameters of the cryo-EM reconstructions of Vif–CBFβ–A3F$_{CTDm}$ complexes and the final model.

a, Fourier shell correlation (FSC) curves of the half maps from gold standard refinements of the Vif–CBFβ–A3F$_{CTDm}$ complex with (cyan) or without (blue) the Vif α-domain and the corresponding interacting CBFβ C-terminus. The FSC curve of the map and final model of the truncated Vif–CBFβ–A3F$_{CTDm}$ complex is in green. Resolution of the maps are determined by the cutoff values at FSC = 0.143. **b**, The Euler angle distribution of the classified particles of the truncated Vif–CBFβ–A3F$_{CTDm}$ complex used for the final 3D reconstruction. **c**, Color coded local resolution estimation of the D2 symmetrized map of the truncated Vif–CBFβ–A3F$_{CTDm}$ complex.

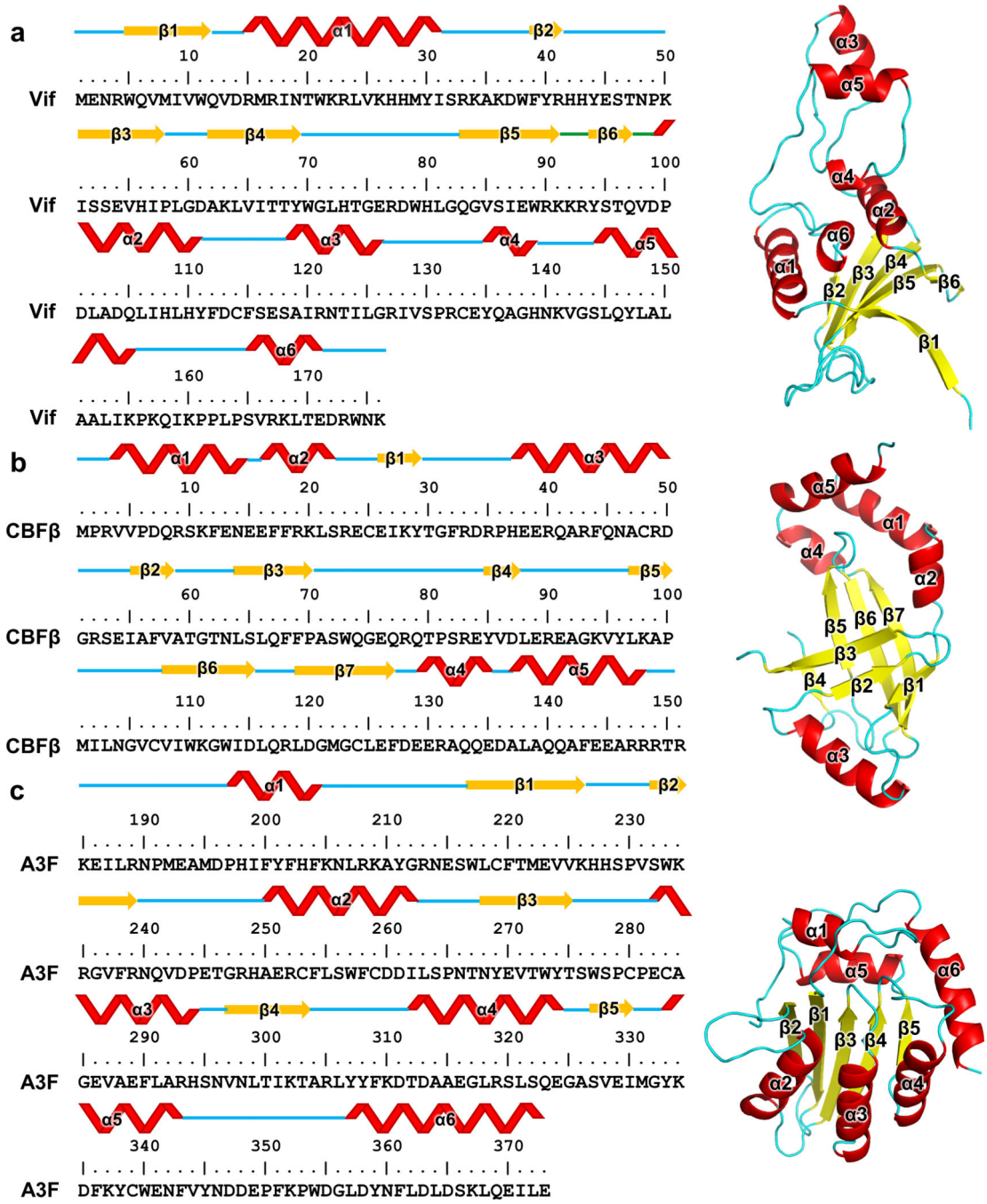

Extended Data Fig. 10. The detailed illustrations of the secondary structure elements of Vif176 (a), CBFβ151 (b) and A3F$_{CTD}$ (c).

The secondary structures are annotated on primary amino acid sequences (left) and tertiary structures (right). The tertiary structures for illustration are: Vif, extracted from PDB 4N9F; CBFβ151, extracted from our cryo-EM structure; A3F$_{CTD,}$ PDB 3WUS.

Supplementary Material

Refer to Web version on PubMed Central for supplementary material.

Acknowledgements

We thank S. Wu, M. Llaguno and X. Liu at Yale Cryo-EM facilities and C. Wang and J. Liu for assistance with data collection. We thank K. Knecht, O. Buzovetsky, S. C. Devarkar and other Xiong lab members for discussions. This work was supported by National Institutes of Health grant AI116313 (Y.X.). This work was supported in part by the Intramural Research Program of the NIH, National Cancer Institute, Center for Cancer Research, and by Intramural AIDS Targeted Antiviral Program grant and Innovation Fund, Office of AIDS Research, NIH to V.K.P.

References

1. Lecossier D, Bouchonnet F, Clavel F & Hance AJ Hypermutation of HIV-1 DNA in the absence of the Vif protein. Science 300, 1112 (2003). [PubMed: 12750511]
2. Mangeat B, et al. Broad antiretroviral defence by human APOBEC3G through lethal editing of nascent reverse transcripts. Nature 424, 99–103 (2003). [PubMed: 12808466]
3. Zhang H, et al. The cytidine deaminase CEM15 induces hypermutation in newly synthesized HIV-1 DNA. Nature 424, 94–98 (2003). [PubMed: 12808465]
4. Jager S, et al. Vif hijacks CBF-beta to degrade APOBEC3G and promote HIV-1 infection. Nature 481, 371–375 (2011). [PubMed: 22190037]
5. Zhang W, Du J, Evans SL, Yu Y & Yu XF T-cell differentiation factor CBF-beta regulates HIV-1 Vif-mediated evasion of host restriction. Nature 481, 376–379 (2011). [PubMed: 22190036]
6. Marin M, Rose KM, Kozak SL & Kabat D HIV-1 Vif protein binds the editing enzyme APOBEC3G and induces its degradation. Nat Med 9, 1398–1403 (2003). [PubMed: 14528301]
7. Sheehy AM, Gaddis NC & Malim MH The antiretroviral enzyme APOBEC3G is degraded by the proteasome in response to HIV-1 Vif. Nat Med 9, 1404–1407 (2003). [PubMed: 14528300]
8. Stopak K, de Noronha C, Yonemoto W & Greene WC HIV-1 Vif blocks the antiviral activity of APOBEC3G by impairing both its translation and intracellular stability. Molecular Cell 12, 591–601 (2003). [PubMed: 14527406]
9. Yu X, et al. Induction of APOBEC3G ubiquitination and degradation by an HIV-1 Vif-Cul5-SCF complex. Science 302, 1056–1060 (2003). [PubMed: 14564014]
10. Conticello SG, Harris RS & Neuberger MS The Vif protein of HIV triggers degradation of the human antiretroviral DNA deaminase APOBEC3G. Curr Biol 13, 2009–2013 (2003). [PubMed: 14614829]
11. Conticello SG, Thomas CJ, Petersen-Mahrt SK & Neuberger MS Evolution of the AID/APOBEC family of polynucleotide (deoxy)cytidine deaminases. Mol Biol Evol 22, 367–377 (2005). [PubMed: 15496550]
12. Feng Y, Baig TT, Love RP & Chelico L Suppression of APOBEC3-mediated restriction of HIV-1 by Vif. Front Microbiol 5, 450 (2014). [PubMed: 25206352]
13. Chaipan C, Smith JL, Hu WS & Pathak VK APOBEC3G restricts HIV-1 to a greater extent than APOBEC3F and APOBEC3DE in human primary CD4+ T cells and macrophages. J Virol 87, 444–453 (2013). [PubMed: 23097438]
14. Navarro F, et al. Complementary function of the two catalytic domains of APOBEC3G. Virology 333, 374–386 (2005). [PubMed: 15721369]
15. Russell RA, Smith J, Barr R, Bhattacharyya D & Pathak VK Distinct Domains within APOBEC3G and APOBEC3F Interact with Separate Regions of Human Immunodeficiency Virus Type 1 Vif. Journal of Virology 83, 1992–2003 (2009). [PubMed: 19036809]
16. Smith JL & Pathak VK Identification of specific determinants of human APOBEC3F, APOBEC3C, and APOBEC3DE and African green monkey APOBEC3F that interact with HIV-1 Vif. J Virol 84, 12599–12608 (2010). [PubMed: 20943965]
17. Hache G, Liddament MT & Harris RS The retroviral hypermutation specificity of APOBEC3F and APOBEC3G is governed by the C-terminal DNA cytosine deaminase domain. J Biol Chem 280, 10920–10924 (2005). [PubMed: 15647250]
18. Aydin H, Taylor MW & Lee JE Structure-guided analysis of the human APOBEC3-HIV restrictome. Structure 22, 668–684 (2014). [PubMed: 24657093]

19. Kitamura S, Ode H & Iwatani Y Structural Features of Antiviral APOBEC3 Proteins are Linked to Their Functional Activities. Front Microbiol 2, 258 (2011). [PubMed: 22203821]
20. Russell RA & Pathak VK Identification of two distinct human immunodeficiency virus type 1 Vif determinants critical for interactions with human APOBEC3G and APOBEC3F. J Virol 81, 8201–8210 (2007). [PubMed: 17522216]
21. Fribourgh JL, et al. Core binding factor beta plays a critical role by facilitating the assembly of the Vif-cullin 5 E3 ubiquitin ligase. J Virol 88, 3309–3319 (2014). [PubMed: 24390320]
22. Kim DY, et al. CBFbeta stabilizes HIV Vif to counteract APOBEC3 at the expense of RUNX1 target gene expression. Mol Cell 49, 632–644 (2013). [PubMed: 23333304]
23. Guo Y, et al. Structural basis for hijacking CBF-beta and CUL5 E3 ligase complex by HIV-1 Vif. Nature 505, 229–233 (2014). [PubMed: 24402281]
24. Bohn MF, et al. Crystal structure of the DNA cytosine deaminase APOBEC3F: the catalytically active and HIV-1 Vif-binding domain. Structure 21, 1042–1050 (2013). [PubMed: 23685212]
25. He Z, Zhang W, Chen G, Xu R & Yu XF Characterization of conserved motifs in HIV-1 Vif required for APOBEC3G and APOBEC3F interaction. J Mol Biol 381, 1000–1011 (2008). [PubMed: 18619467]
26. Pery E, Rajendran KS, Brazier AJ & Gabuzda D Regulation of APOBEC3 proteins by a novel YXXL motif in human immunodeficiency virus type 1 Vif and simian immunodeficiency virus SIVagm Vif. J Virol 83, 2374–2381 (2009). [PubMed: 19109396]
27. Nakashima M, et al. Structural Insights into HIV-1 Vif-APOBEC3F Interaction. Journal of Virology 90, 1034–1047 (2016). [PubMed: 26537685]
28. Yamashita T, Kamada K, Hatcho K, Adachi A & Nomaguchi M Identification of amino acid residues in HIV-1 Vif critical for binding and exclusion of APOBEC3G/F. Microbes Infect 10, 1142–1149 (2008). [PubMed: 18603011]
29. Dang Y, Davis RW, York IA & Zheng YH Identification of 81LGxGxxIxW89 and 171EDRW174 domains from human immunodeficiency virus type 1 Vif that regulate APOBEC3G and APOBEC3F neutralizing activity. J Virol 84, 5741–5750 (2010). [PubMed: 20335268]
30. Kitamura S, et al. The APOBEC3C crystal structure and the interface for HIV-1 Vif binding. Nat Struct Mol Biol 19, 1005–1010 (2012). [PubMed: 23001005]
31. Albin JS, et al. A single amino acid in human APOBEC3F alters susceptibility to HIV-1 Vif. J Biol Chem 285, 40785–40792 (2010). [PubMed: 20971849]
32. Siu KK, Sultana A, Azimi FC & Lee JE Structural determinants of HIV-1 Vif susceptibility and DNA binding in APOBEC3F. Nat Commun 4, 2593 (2013). [PubMed: 24185281]
33. Anderson BD & Harris RS Transcriptional regulation of APOBEC3 antiviral immunity through the CBF-beta/RUNX axis. Sci Adv 1, e1500296 (2015). [PubMed: 26601257]
34. Dang Y, Wang X, Zhou T, York IA & Zheng YH Identification of a novel WxSLVK motif in the N terminus of human immunodeficiency virus and simian immunodeficiency virus Vif that is critical for APOBEC3G and APOBEC3F neutralization. J Virol 83, 8544–8552 (2009). [PubMed: 19535447]
35. Chen G, He Z, Wang T, Xu R & Yu XF A patch of positively charged amino acids surrounding the human immunodeficiency virus type 1 Vif SLVx4Yx9Y motif influences its interaction with APOBEC3G. J Virol 83, 8674–8682 (2009). [PubMed: 19535450]
36. Kim DY The assembly of Vif ubiquitin E3 ligase for APOBEC3 degradation. Arch Pharm Res 38, 435–445 (2015). [PubMed: 25408426]
37. Richards C, et al. The Binding Interface between Human APOBEC3F and HIV-1 Vif Elucidated by Genetic and Computational Approaches. Cell Reports 13, 1781–1788 (2015). [PubMed: 26628363]
38. LaRue RS, et al. Guidelines for naming nonprimate APOBEC3 genes and proteins. J Virol 83, 494–497 (2009). [PubMed: 18987154]
39. Nakashima M, et al. Mapping Region of Human Restriction Factor APOBEC3H Critical for Interaction with HIV-1 Vif. J Mol Biol 429, 1262–1276 (2017). [PubMed: 28336404]
40. Huthoff H & Malim MH Identification of amino acid residues in APOBEC3G required for regulation by human immunodeficiency virus type 1 Vif and Virion encapsidation. J Virol 81, 3807–3815 (2007). [PubMed: 17267497]

41. Bogerd HP, Doehle BP, Wiegand HL & Cullen BR A single amino acid difference in the host APOBEC3G protein controls the primate species specificity of HIV type 1 virion infectivity factor. Proc Natl Acad Sci U S A 101, 3770–3774 (2004). [PubMed: 14999100]
42. Mangeat B, Turelli P, Liao S & Trono D A single amino acid determinant governs the species-specific sensitivity of APOBEC3G to Vif action. J Biol Chem 279, 14481–14483 (2004). [PubMed: 14966139]
43. Schrofelbauer B, Chen D & Landau NR A single amino acid of APOBEC3G controls its species-specific interaction with virion infectivity factor (Vif). Proc Natl Acad Sci U S A 101, 3927–3932 (2004). [PubMed: 14978281]
44. Xu H, et al. A single amino acid substitution in human APOBEC3G antiretroviral enzyme confers resistance to HIV-1 virion infectivity factor-induced depletion. Proc Natl Acad Sci U S A 101, 5652–5657 (2004). [PubMed: 15054139]
45. Kouno T, et al. Structure of the Vif-binding domain of the antiviral enzyme APOBEC3G. Nat Struct Mol Biol 22, 485–491 (2015). [PubMed: 25984970]
46. Britan-Rosich E, Nowarski R & Kotler M Multifaceted counter-APOBEC3G mechanisms employed by HIV-1 Vif. J Mol Biol 410, 1065–1076 (2011). [PubMed: 21763507]
47. Feng Y, Love RP & Chelico L HIV-1 viral infectivity factor (Vif) alters processive single-stranded DNA scanning of the retroviral restriction factor APOBEC3G. J Biol Chem 288, 6083–6094 (2013). [PubMed: 23316055]
48. Duda DM, et al. Structural insights into NEDD8 activation of cullin-RING ligases: conformational control of conjugation. Cell 134, 995–1006 (2008). [PubMed: 18805092]
49. Mehle A, Goncalves J, Santa-Marta M, McPike M & Gabuzda D Phosphorylation of a novel SOCS-box regulates assembly of the HIV-1 Vif-Cul5 complex that promotes APOBEC3G degradation. Genes Dev 18, 2861–2866 (2004). [PubMed: 15574592]
50. Harris RS & Anderson BD Evolutionary Paradigms from Ancient and Ongoing Conflicts between the Lentiviral Vif Protein and Mammalian APOBEC3 Enzymes. PLoS Pathog 12, e1005958 (2016). [PubMed: 27907174]
51. Hache G, Shindo K, Albin JS & Harris RS Evolution of HIV-1 isolates that use a novel Vif-independent mechanism to resist restriction by human APOBEC3G. Curr Biol 18, 819–824 (2008). [PubMed: 18501607]
52. Albin JS, Hache G, Hultquist JF, Brown WL & Harris RS Long-term restriction by APOBEC3F selects human immunodeficiency virus type 1 variants with restored Vif function. J Virol 84, 10209–10219 (2010). [PubMed: 20686027]

Methods-only References

53. Xiao X, Li SX, Yang H & Chen XS Crystal structures of APOBEC3G N-domain alone and its complex with DNA. Nat Commun 7, 12193 (2016). [PubMed: 27480941]
54. Russell RA, Smith J, Barr R, Bhattacharyya D & Pathak VK Distinct domains within APOBEC3G and APOBEC3F interact with separate regions of human immunodeficiency virus type 1 Vif. J Virol 83, 1992–2003 (2009). [PubMed: 19036809]
55. Smith JL, Izumi T, Borbet TC, Hagedorn AN & Pathak VK HIV-1 and HIV-2 Vif Interact with Human APOBEC3 Proteins Using Completely Different Determinants. J Virol (2014).
56. Nguyen KL, et al. Codon optimization of the HIV-1 vpu and vif genes stabilizes their mRNA and allows for highly efficient Rev-independent expression. Virology 319, 163–175 (2004). [PubMed: 15015498]
57. Yee JK, Friedmann T & Burns JC Generation of high-titer pseudotyped retroviral vectors with very broad host range. Methods in cell biology 43 Pt A, 99–112 (1994). [PubMed: 7823872]
58. Unutmaz D, KewalRamani VN, Marmon S & Littman DR Cytokine signals are sufficient for HIV-1 infection of resting human T lymphocytes. J Exp Med 189, 1735–1746 (1999). [PubMed: 10359577]
59. Desimmie BA, Smith JL, Matsuo H, Hu WS & Pathak VK Identification of a tripartite interaction between the N-terminus of HIV-1 Vif and CBFbeta that is critical for Vif function. Retrovirology 14, 19 (2017). [PubMed: 28302150]

60. Mastronarde DN Automated electron microscope tomography using robust prediction of specimen movements. J Struct Biol 152, 36–51 (2005). [PubMed: 16182563]

61. Zheng SQ, et al. MotionCor2: anisotropic correction of beam-induced motion for improved cryo-electron microscopy. Nat Methods 14, 331–332 (2017). [PubMed: 28250466]

62. Zhang K Gctf: Real-time CTF determination and correction. J Struct Biol 193, 1–12 (2016). [PubMed: 26592709]

63. Scheres SH RELION: implementation of a Bayesian approach to cryo-EM structure determination. J Struct Biol 180, 519–530 (2012). [PubMed: 23000701]

64. Scheres SH & Chen S Prevention of overfitting in cryo-EM structure determination. Nat Methods 9, 853–854 (2012). [PubMed: 22842542]

65. Rosenthal PB & Henderson R Optimal determination of particle orientation, absolute hand, and contrast loss in single-particle electron cryomicroscopy. J Mol Biol 333, 721–745 (2003). [PubMed: 14568533]

66. Pettersen EF, et al. UCSF Chimera--a visualization system for exploratory research and analysis. J Comput Chem 25, 1605–1612 (2004). [PubMed: 15264254]

67. Adams PD, et al. PHENIX: a comprehensive Python-based system for macromolecular structure solution. Acta Crystallogr D Biol Crystallogr 66, 213–221 (2010). [PubMed: 20124702]

68. Emsley P, Lohkamp B, Scott WG & Cowtan K Features and development of Coot. Acta Crystallogr D Biol Crystallogr 66, 486–501 (2010). [PubMed: 20383002]

69. Murshudov GN, et al. REFMAC5 for the refinement of macromolecular crystal structures. Acta Crystallogr D Biol Crystallogr 67, 355–367 (2011). [PubMed: 21460454]

70. Afonine PV, et al. New tools for the analysis and validation of cryo-EM maps and atomic models. Acta Crystallogr D Struct Biol 74, 814–840 (2018). [PubMed: 30198894]

71. DeLano W The PyMOL Molecular Graphics System DeLano Scientific, Palo Alto, CA, USA (2002).

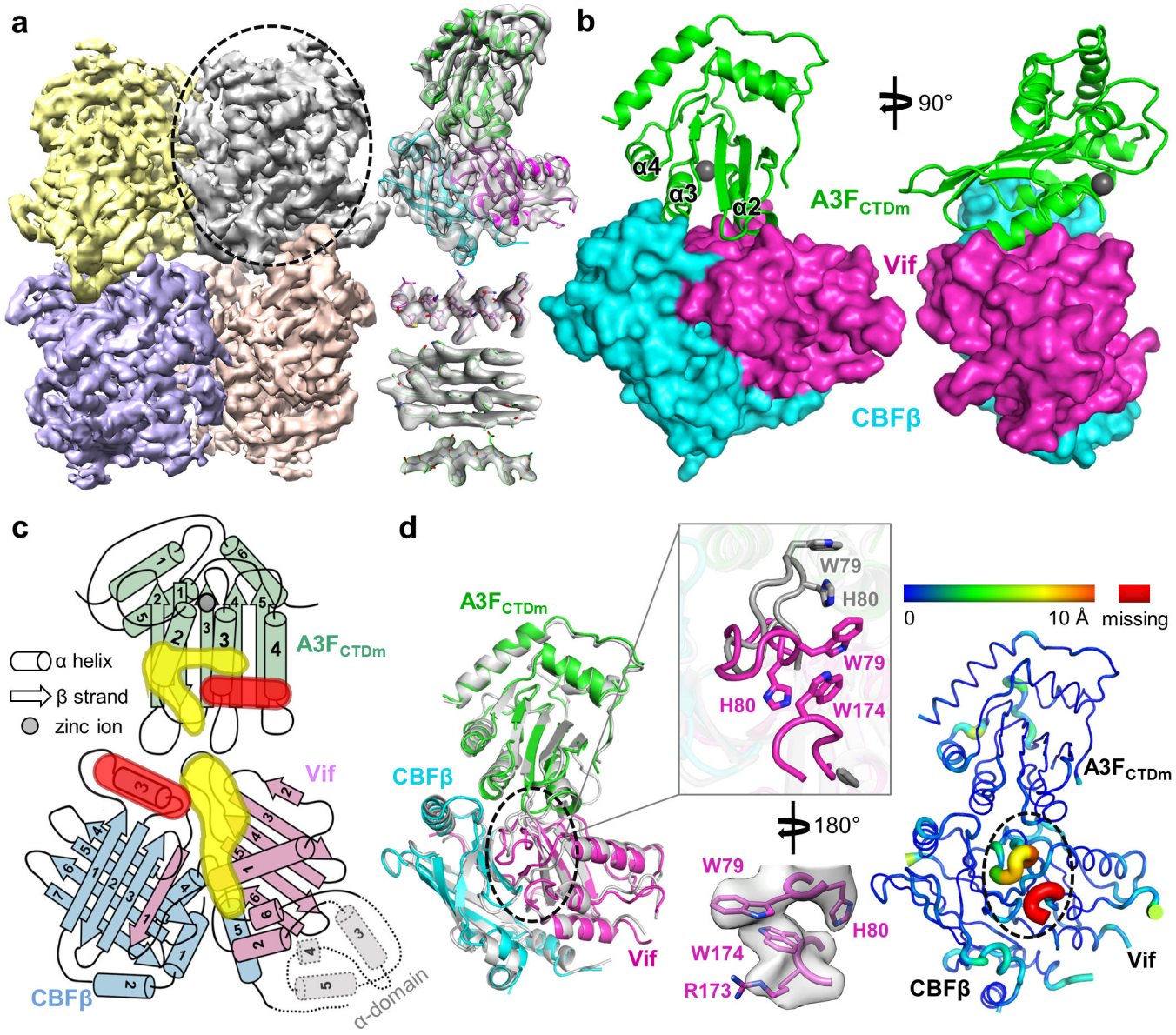

Fig. 1: Vif and CBFβ form a platform for interaction with A3F.

a, **Left,** 3D cryo-EM reconstruction of the Vif–CBFβ–A3F$_{CTDm}$ complex in the tetrameric state at 3.9 Å resolution, with each ternary complex protomer colored differently. Right, the cryo-EM map of one Vif–CBFβ–A3F$_{CTDm}$ ternary complex (oval on left) is shown on top, with examples of high-quality α helix and β sheet/strand regions at the bottom. **b**, Overall structure of one Vif–CBFβ–A3F$_{CTDm}$ ternary complex in two orthogonal views. Vif (magenta) and CBFβ (cyan) form a wedge-like platform for A3F$_{CTDm}$ (green) to dock primarily via one end of its α-helical surface, distal from the zinc-containing catalytic site (red sphere). **c**, Cartoon illustration of the A3F$_{CTDm}$ and Vif/CBFβ secondary structures, with the CBFβ-A3F$_{CTDm}$ interface highlighted in red and the Vif-A3F$_{CTDm}$ interface in yellow. The α helices are represented by cylinders, β strands by arrows, and the zinc ion by a circle. The deleted small α-domain (grey) of Vif and the corresponding interacting CBFβ C-terminus are contoured by dash lines. The detailed annotations of the secondary structure

elements are illustrated in Extended Data Fig. 10. **d**, Majority of Vif–CBFβ and $A3F_{CTDm}$ maintain their conformations upon ternary complex formation. Left, superposition of the ternary structure with individual $A3F_{CTD}$ (PDB 3WUS, grey) and Vif–CBFβ portion from the Vif–E3 ligase structure (PDB 4N9F, grey). The major local conformational changes are circled, with details (top) and the observed cryo-EM map (bottom) shown in the middle inset. Right, the rainbow putty representation of the superposition. The color spectrum and the coil thickness represent the deviation of the aligned Cα atoms in the structures, which varies from 0 Å (blue) to ~10 Å (orange). The Vif C-terminal region residues 173–176 missing in the Vif-E3 ligase structure [23] are colored in red.

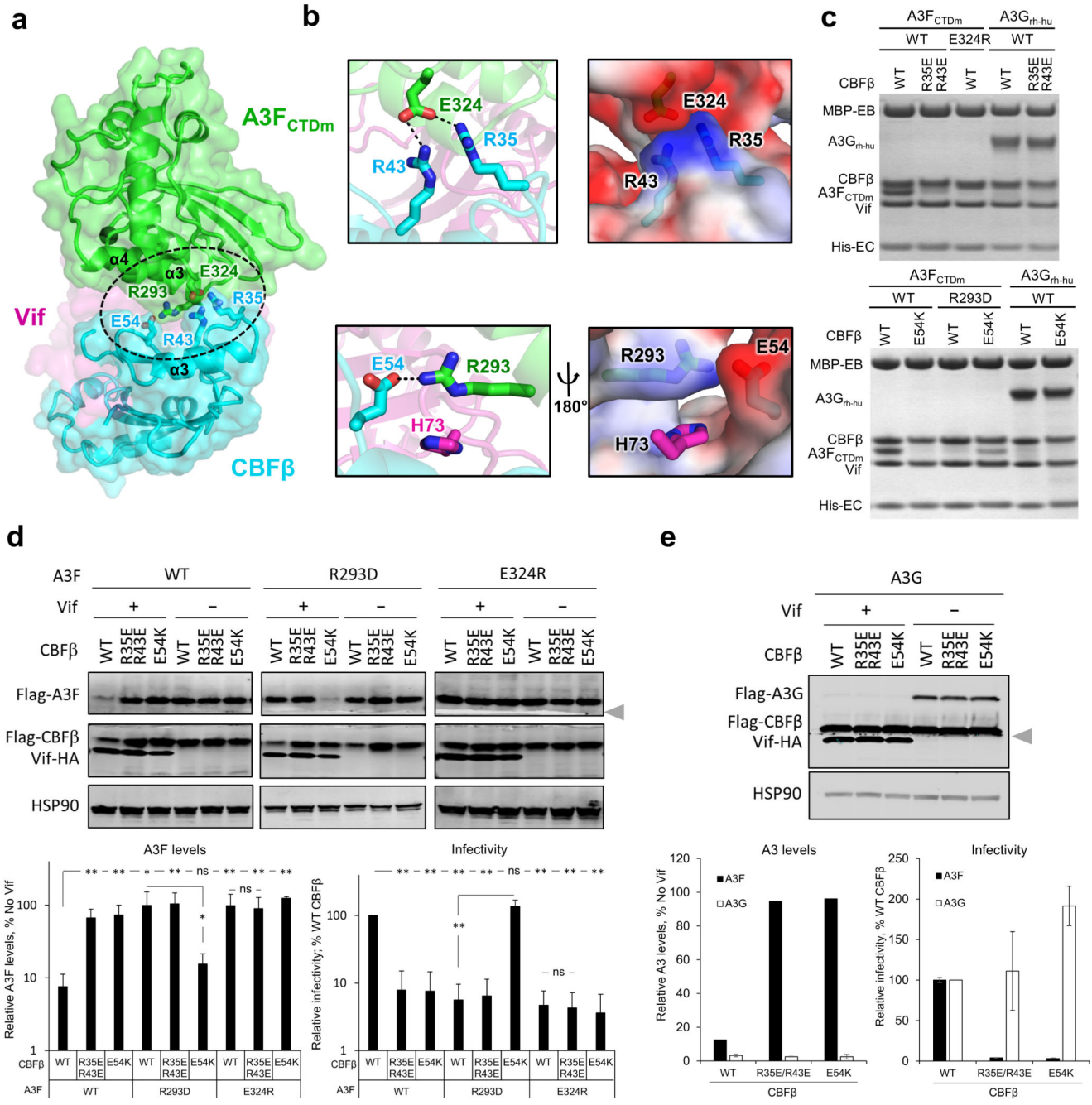

Fig. 2: The CBFβ-A3F interface is important for Vif–CBFβ–A3F complex formation, Vif-mediated A3F degradation, and viral infectivity.

a, Overview of the CBFβ-A3F$_{CTDm}$ interface (oval) with the critical interacting residues highlighted as sticks. The zinc atom is shown as red sphere. **b**, Detailed illustrations of the interacting residues and the electrostatic complementation at the interface. Blue, positively charged; red, negatively charged. **c,** Mutational analysis of the interactions by an *in vitro* binding assay using MBP-tagged Vif–CBFβ–EloB–EloC variants to pulldown A3F$_{CTDm}$ variants or A3G$_{rh-hu}$. WT, wild type. The loading controls are shown in Supplementary Fig. 1a & c. **d**, Analysis of the critical interacting residues at the CBFβ-A3F interface in cell-

based Vif-mediated A3F degradation and infectivity assays (mean ± s.d.; n=4 biologically independent experiments). The blot was cut as indicated (gray arrow), with one part probed for Flag-A3F and HSP90, and the other for Flag-CBFβ and Vif-HA. **e**, The A3F-interacting CBFβ residues are not critical for Vif-mediated A3G degradation (mean ± s.d.; n=3 biologically independent experiments for A3G). The blot was analyzed as in **d**; the Flag-CBFβ band was partially cut and could be detected in both parts by the same anti-Flag antibody. Statistical significance of A3 degradation and infectivity was assessed by two-tailed *t*-test assuming equal variance; *, $P < 0.05$; **, $P < 0.005$; ns, *p*-value not significant. Uncropped images and data behind graphs are available as Source Data.

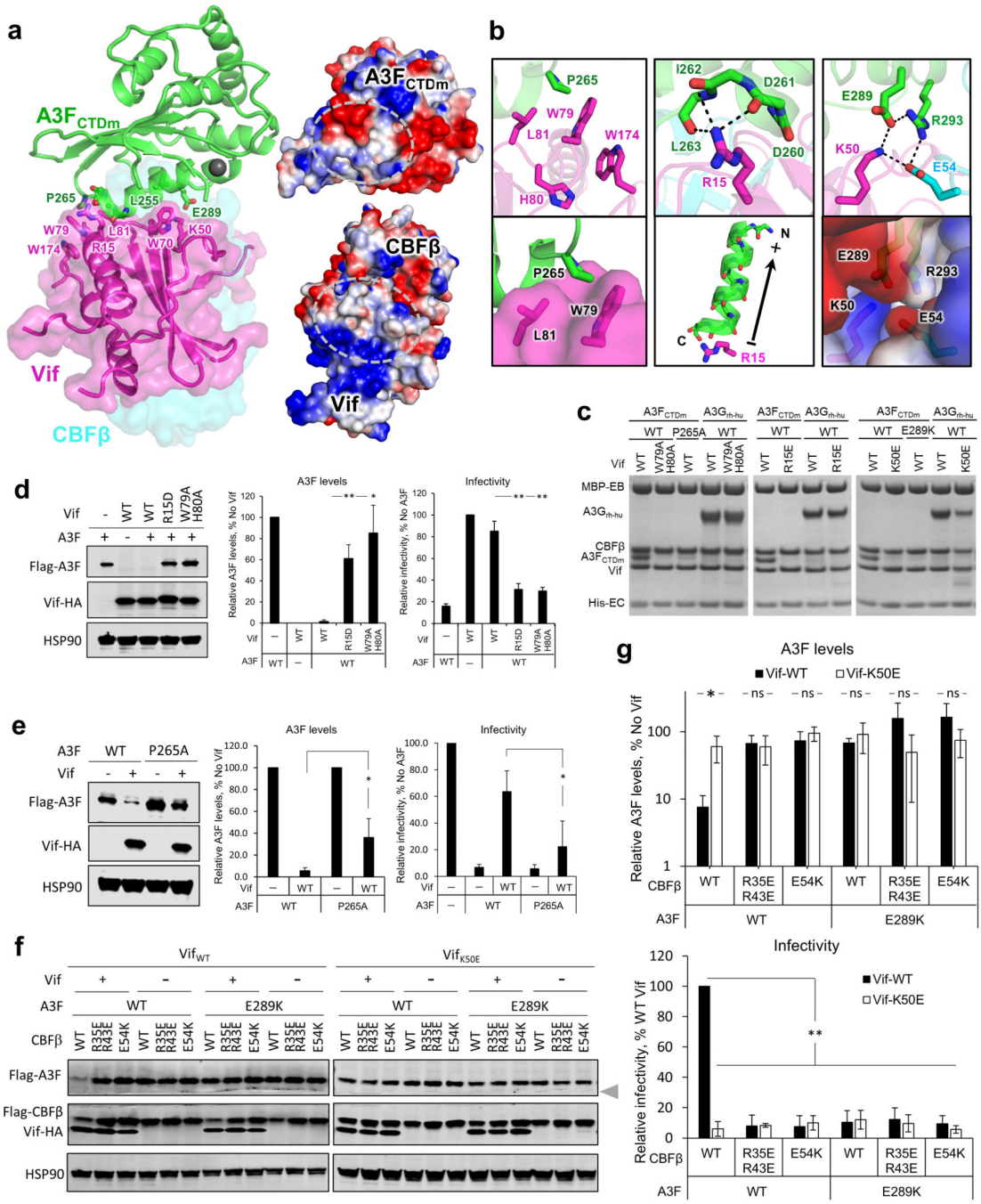

Fig. 3: The Vif-A3F interface is critical for Vif–CBFβ–A3F complex formation, Vif-mediated A3F degradation, and viral infectivity.

a, Left, overview of the Vif-A3F$_{CTDm}$ interface with the interacting residues highlighted as sticks. The zinc atom is shown as red sphere. Right, the overall electrostatic potential surfaces for Vif/CBFβ and A3F$_{CTDm}$ with the Vif-A3F$_{CTDm}$ interaction interfaces circled. Blue, positively charged; red, negatively charged; white, hydrophobic. **b**, Detailed illustrations of the critical interacting residues at the Vif-A3F$_{CTDm}$ interface. The electrostatic interactions are indicated with dashed lines. The cumulative dipole effect of A3F$_{CTDm}$ α2 helix from C-terminus to N-terminus is indicated by an arrow (lower middle).

c, Mutational analysis of the interactions by an *in vitro* binding assay using MBP-tagged Vif–CBFβ–EloB–EloC variants to pulldown $A3F_{CTDm}$ variants or $A3G_{rh\text{-}hu}$. WT, wild type. The loading controls are shown in Supplementary Fig. 1b & c. **d, e**, Mutagenesis analysis of critical interacting residues at the Vif-A3F interface in cell-based Vif-mediated A3F degradation and infectivity assays (mean ± s.d.; n=3 biologically independent experiments). Vif mutants are shown in d, A3F mutant is shown in e. **f, g**, Analysis of $A3F_{E289K}$, Vif_{K50E} and $CBF\beta_{E54K}$ mutants on Vif-mediated A3F degradation and infectivity (mean ± s.d.; n=4 biologically independent experiments). The blot was cut as indicated (gray arrow), where one part was probed for Flag-A3F and HSP90, and the other for Flag-CBFβ and Vif-HA. Statistical significance of A3 degradation and infectivity was assessed by two-tailed *t*-test assuming equal variance; *, $P < 0.05$; **, $P < 0.005$; ns, *p*-value not significant. Uncropped images and data behind graphs are available as Source Data.

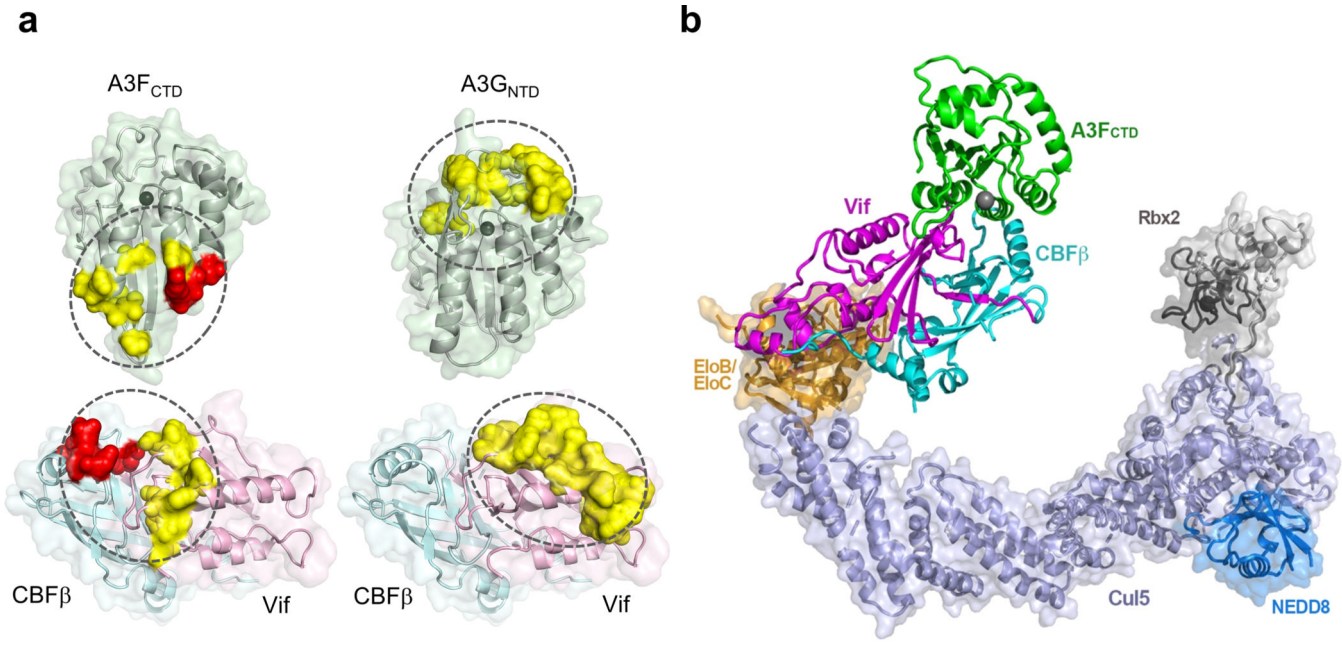

Fig. 4: Models of A3-Vif/CBFβ interactions and the Vif–CBFβ–Cul5 E3–A3F$_{CTD}$ complex.

a, Comparison of the Vif/CBFβ-A3 interfaces (ovals) for A3F$_{CTD}$ (left) and A3G$_{NTD}$ (homology model built from rhesus A3G$_{NTD}$ (PDB 5K81), right). Critical residues observed at the CBFβ-A3F interface are highlighted as red surfaces, critical residues at the observed Vif-A3F interface and the predicted Vif-A3G interface [39–45] are highlighted in yellow. The zinc ion at the ssDNA binding or catalytic site is shown as a dark gray sphere. **b**, A comprehensive picture of the fully assembled Vif–CBFβ–Cul5 E3–A3F$_{CTD}$ complex structure by overlaying the Vif–CBFβ portion from the current ternary complex and that of the Vif–E3 ligase complex (PDB 4N9F) structures, along with the separately determined Cul5$_{CTD}$–Rbx2 (PDB 3DPL) and Cul5$_{CTD}$–NEDD8–Rbx1 (PDB 3DQV) structures. The N-terminal of A3F$_{CTD}$ labelled as “N”, is exposed in a geometry that can accommodate A3F$_{NTD}$.

TABLE 1

Cryo-EM data collection, refinement and validation statistics

	Vif176Δ114–157–A3F$_{CTDm}$-40-CBFβ151 (EMD-9380, PDB 6NIL)		Vif176–A3F$_{CTDm}$-40-CBFβ187 (EMD-9381)
Data collection and processing	1	2/3	1
Magnification	130,000		130,000
Voltage (kV)	300		300
Electron exposure (e^{-}/Å^2)	~56	61/56	59
Defocus range (μm)	−1.2 to −2.9	−1.7 to −3.7/ −1.5 to −3.2	−0.9 to −2.9
Pixel size (Å)	1.05		1.05
Stage tilting (°)	0	−30/−30	−30
Symmetry imposed	D2		D2
Initial particle images (no.)	1243243 (untilt) / 1197365 (tilt)		1140691
Final particle images (no.)	337256		165629
Map resolution (Å)	3.9		5
FSC threshold	0.143		0.143
Map resolution range (Å)	3.7–4.6		-
Refinement			
Initial model used (PDB code)	4N9F, 3WUS		-
Model resolution (Å)	3.9		-
FSC threshold	0.5		
Model resolution range (Å)	3.9–113.4		-
Map sharpening *B* factor (Å^2)	−223		−359
Model composition			
Nonhydrogen atoms	15216		-
Protein residues	1800		-
Ligands	Zn, 4		-
B factors (Å^2)			
Protein	113		-
Ligand	343		-
R.m.s. deviations			
Bond lengths (Å)	0.005		-
Bond angles (°)	1.0		-
Validation			
MolProbity score	1.67		-
Clashscore	3		-
Poor rotamers (%)	0.99		-
Ramachandran plot			
Favored (%)	90.4		-

	Vif176Δ114–157–A3F$_{CTDm}$-40-CBFβ151 (EMD-9380, PDB 6NIL)	Vif176–A3F$_{CTDm}$-40-CBFβ187 (EMD-9381)
Allowed (%)	9.6	-
Disallowed (%)	0	-